JOURNAL OF AIRCRAFT
Vol. 43, No. 3, May–June 2006

Aeroelasticity of Nonlinear Structures Using the Corotational Method

Ana Relvas[*] and Afzal Suleman[†]
IDMEC-Instituto Superior Técnico, 1049-001 Lisbon, Portugal

A method to solve aeroelasticity of geometrically nonlinear structures in the time domain is presented. Large structural deformations are taken into account using the nonlinear corotational theory. Stable and accurate nonlinear solutions are obtained using the corotational theory in combination with an implicit energy-conserving algorithm. The fluid flow is modeled using Euler equations solved using a modified multiple moving-frames method. The application of the proposed methodology is illustrated on a study of nonlinear aeroelastic response of a NACA0012 airfoil in transonic flow. The proposed method is stable and results in accurate nonlinear solutions without the need to deform or regenerate the fluid grid.

Nomenclature

$\hat{\boldsymbol{A}}$ = $\partial\hat{\boldsymbol{E}}/\partial\hat{\boldsymbol{Q}}$ Jacobian matrix

$\boldsymbol{a}, \boldsymbol{a}_{jk}$ = acceleration vector of fluid flow particle jk relative to the absolute reference frame

$\boldsymbol{a}_j$ = $\{a_{j_x}, a_{j_y}\}$ translational acceleration vector of moving frame j

$\boldsymbol{a}_t, \boldsymbol{a}_{t,jk}$ = transformation acceleration vector of fluid flow particle jk

a_∞ = freestream sound speed

$\hat{\boldsymbol{a}}, \hat{\boldsymbol{a}}_{jk}$ = acceleration vector of fluid flow particle jk relative to the moving reference frame j

$\hat{\boldsymbol{B}}$ = $\partial\hat{\boldsymbol{F}}/\partial\hat{\boldsymbol{S}}$ Jacobian matrix

b = airfoil semichord

C_l = lift coefficient

C_m = moment coefficient

$\hat{\boldsymbol{D}}$ = $\partial\hat{\boldsymbol{S}}/\partial\hat{\boldsymbol{Q}}$ Jacobian matrix

$\boldsymbol{d}$ = $[u, v]$ finite element translational degrees of freedom

E = Young's modulus

E = finite element cross-sectional area

$(\boldsymbol{e}, \boldsymbol{b})$ = current finite element local coordinate system

$\hat{e}$ = total fluid flow energy relative to the moving reference frame

$\boldsymbol{F}$ = vector of applied forces on the airfoil

$\boldsymbol{F}_a$ = aerodynamic force vector applied on the airfoil

$\boldsymbol{F}_k$ = force vector applied on the airfoil as a result of springs reactions

$\hat{\boldsymbol{F}}$ = flux vector relative to the moving reference frame

$\boldsymbol{f}_e$ = external force vector

$\boldsymbol{f}_i$ = internal force vector

$\boldsymbol{f}_{\mathrm{Li}}$ = $[N, M_1, M_2]$ local internal force vector

h = $\theta\Delta t/(1+\varphi)$

h = airfoil plunge degree of freedom

I_α = airfoil polar moment of inertia about the elastic axis

J^{-1} = fluid grid metric Jacobian

$\boldsymbol{K}$ = airfoil stiffness matrix

$\boldsymbol{K}_l$ = finite element linear stiffness matrix

$\boldsymbol{K}_T$ = finite element total nonlinear stiffness matrix

$\boldsymbol{K}_{t\sigma}$ = finite element "geometric" stiffness matrix

l_c = length of finite element current configuration

l_0 = length of finite element initial configuration

$\boldsymbol{M}$ = airfoil mass matrix, finite element mass matrix

M_∞ = freestream Mach number

m = airfoil mass

p = fluid flow pressure

$\boldsymbol{p}$ = $\{u_1, v_1, \theta_1, u_2, v_2, \theta_2\}$ finite element degree of freedom vector

$\boldsymbol{p}_L$ = $\{0, 0, \theta_{L1}, u_L, 0, \theta_{L2}\}$ finite element local degree of freedom vector

$\hat{\boldsymbol{Q}}$ = vector of conservative flow variables

$\boldsymbol{q}$ = $\{h/2b, \alpha\}$ degrees of freedom of the airfoil rigid-body motion

$\boldsymbol{r}, \boldsymbol{r}_{jk}$ = position vector of fluid flow particle jk relative to the absolute frame of reference

$\boldsymbol{r}_j$ = origin coordinates of reference frame j

$r_{j,k}$ = distance between the grid point jk and the airfoil middle chord

$\hat{\boldsymbol{r}}, \hat{\boldsymbol{r}}_{jk}$ = $\{\hat{x}, \hat{y}\}$ fluid flow particle jk position vector relative to the moving frame j

$\hat{\boldsymbol{S}}$ = right hand side of the modified Euler equations

$\boldsymbol{T}$ = finite element corotational transformation matrix

$\boldsymbol{T}_\eta$ = matrix which columns are matrix $\hat{\boldsymbol{B}}$ eigenvectors

$\boldsymbol{T}_\xi$ = matrix which columns are matrix $\hat{\boldsymbol{A}}$ eigenvectors

t^* = $ta_\infty/2b$ dimensionless time

U_∞ = freestream velocity

U^* = $U_\infty/b\omega_\alpha$

$\hat{U}, \hat{V}$ = contravariant velocity components relative to the moving frame

u_1, v_1, θ_1 = finite element node 1 deg of freedom (translations and rotation)

u_2, v_2, θ_2 = finite element node 2 deg of freedom (translations and rotation)

$\boldsymbol{V}, \boldsymbol{V}_{jk}$ = fluid flow particle jk velocity vector relative to the absolute reference frame

$\boldsymbol{V}_j$ = $\{v_{j_x}, v_{j_y}\}$ moving frame j translational velocity vector

$\boldsymbol{V}_t, \boldsymbol{V}_{t,jk}$ = fluid flow particle jk transformation velocity

$\hat{\boldsymbol{V}}, \hat{\boldsymbol{V}}_{jk}$ = $\{\hat{u}, \hat{v}\}$, $\{\hat{u}_{jk}, \hat{v}_{jk}\}$ velocity vector of fluid flow particle jk relative to the moving frame j

---

Received 16 January 2005; revision received 22 June 2005; accepted for publication 12 July 2005.

[*] Ph.D. Candidate, Department of Engineering Mecânica, Sec. Aeroespacial, Avenue Rovisco Pais; anarelvas@ist.utl.pt. Student Member AIAA.

[†] Associate Professor, Department of Engineering Mecânica, Sec. Aeroespacial, Avenue Rovisco Pais; currently Professor, University of Victoria, Department of Mechanical Engineering, Victoria, BC, Canada; suleman@ist.utl.pt. Associate Fellow AIAA.

(X, Y) = fixed reference frame

$\boldsymbol{X}_1, \boldsymbol{X}_2$ = coordinates of nodes 1 and 2 of the initial finite element

x_α = distance in semichord measured from the elastic axis to the center of mass

$(\hat{x}_j, \hat{y}_j)$ = moving frame associated with fluid flow grid node j

α = airfoil pitch degree of freedom

α = beam rigid rotation angle

γ = 1.4, ratio of specific heat

γ_α^2 = I_α/mb^2

Δt = time step

θ = constant of fluid flow solver scheme

$\boldsymbol{\Lambda}_\eta$ = diagonal matrix with matrix $\hat{\boldsymbol{B}}$ eigenvalues

$\boldsymbol{\Lambda}_\xi$ = diagonal matrix with matrix $\hat{\boldsymbol{A}}$ eigenvalues

μ = $m/\pi\rho b^2$ airfoil air-mass ratio

ξ, η = curvilinear coordinates of fluid grid

$\xi_{\hat{x}}, \xi_{\hat{y}}, \eta_{\hat{x}}, \eta_{\hat{y}}$ = fluid flow grid transformation metrics

ρ = fluid flow density

φ = constant of fluid flow solver scheme

ω_h = plunge motion uncoupled natural frequency

$\boldsymbol{\omega}_j$ = moving frame j angular velocity vector

$\dot{\boldsymbol{\omega}}_j$ = angular acceleration vector of moving frame j

ω_α = pitch motion uncoupled natural frequency

I. Introduction

FLUID-STRUCTURE-INTERACTION (FSI) algorithms solve problems characterized by the coupling between the fluid and the structural fields. Aeroelasticity is one possible application of FSI techniques. Nonlinear aeroelasticity is a complex phenomenon where nonlinearities such as large structural deformations, material nonlinearities, shock waves, separation, and viscous effects play an important role. A detailed discussion about the physical sources of nonlinearities is presented by Dugundji[1] and Dowell et al.[2]

Linear aeroelastic analysis can be considered as a mature science; however, its assumptions might not be accurate enough for certain flight regime requirements. Linear theories can lead to overly conservative flutter margins and design of vehicles with suboptimal performance. Situations where the linear theory is not reliable are the prediction of the transonic dip and in the design of aircraft with high-aspect-ratio wings where the geometrically nonlinear structural effects play a crucial role. Thus, assuming small aeroelastic perturbations and using lower-order fluid and linear structural models might not be acceptable in some aircraft configurations being currently considered.

Currently, nonlinear aeroelastic methods are not fully developed, and one major problem is the high computational cost associated. Most of the methods solve the problem in the time domain because frequency-domain methods are not able to predict chaotic behavior,[3] and also, the time domain is more amenable to state-space control methodologies.[4] Thus, the development of general, computationally efficient, robust, and accurate nonlinear aeroelastic algorithms is needed to properly design for nonlinear aeroelastic response of flexible aircraft structures.[5]

Most of the reported literature on nonlinear aeroelasticity has focused on improving fluid flow modeling using nonlinear models for Euler and Navier–Stokes equations.[6–11] Some work considering nonlinear structures has also been reported.[12–14] The limit-cycle-oscillations nonlinear phenomenon was studied by Tang et al.[15] and Weiliang and Dowell.[16] Research reporting different sources of nonlinearity has been presented by Dowell and Tang.[17] Also, computational and experimental investigation on limit-cycle oscillations was performed by Sheta et al.,[18] and results highlight the importance of including nonlinearities in both structures and fluid solvers.

As the structure deforms, the fluid grid has to be regenerated or deformed to agree with the boundary change. This can be one of the most time-consuming steps within the fluid-structure-interaction algorithm, and it can also introduce errors if the fluid grid cell has unacceptable distortion. An overview of the methods applied in aeroelasticity to deal with the fluid grid adjustment is presented by Piperno.[19] One possible approach is the use of algebraic methods,[20] which redistribute the grid nodes deforming an existing grid. They are fast but are limited to problems with small deformations because large deformations can lead to poor quality grids and grid lines cross over. One of the most commonly used methods is the arbitrary Lagrangian Eulerian formulation (ALE). Here, besides the material domain, associated with the Lagrangian description, and the spatial domain, associated with the Eulerian description, there is a reference domain associated with the computational mesh, which has a determined motion different from the material and the spatial domains. In short, the grid points can be displaced independently of the fluid motion, and the fluid grid nodes remain attached to the structure nodes as the structure deforms. This formulation requires an extra grid-deformation algorithm. The ALE is an elegant and simple formulation, which allows to study complex geometries even using unstructured meshes. The solving algorithm is split in two steps: determination of the Lagrangian and of the convective fluxes, which excludes global upwind schemes and limits the time step to small values. Some applications of the ALE to aeroelasticity can be found in Refs. 21–25. In different ways, all of these methods have in common the idea of accommodating the fluid grid to the structure deformation, and all have a computational time associated proportional with the level of generality and stability. One of the methods reported by Piperno[19] is the moving-frames method originally proposed by Kandil and Chuang[26,27] for problems with rigid structures and by Farhat and Lin[28] and Lin[29] for problems with flexible structures. This method does not require any fluid grid deformation or regeneration, and it is based on the idea of solving the fluid flow equations with respect to multiple moving frames that follow the structure. This theory allows one to obtain fluid-structure interaction solutions with no mesh deformation or regeneration; however, Farhat and Lin[28] and Lin[29] have reported that it is only suitable to problems with small deformations.

The nonlinear corotational finite element theory solves problems of geometrically nonlinear structures, and it is based on the following idea: one finite element displacement is considered to be composed of the element initial configuration rigid motion, which results in the corotated element and of the corotated element small deformation. This information naturally couples with the fluid algorithm presented and as the corotational theory decomposes the displacement in a manner that the elastic deformation determined is always small, the moving-frames algorithm does not fail. Thus, an efficient, stable, and accurate nonlinear method is obtained.

Furthermore, the nonlinear corotational finite element technique's main advantage is making it possible to use finite element linear codes already developed to obtain geometrically nonlinear solutions. A cantilever plate subjected to a low-speed fluid flow was successfully studied using the corotational theory in combination with an implicit-energy-conserving algorithm[30] to solve the structural dynamic equations.

Here, a staggered fluid-structure-interaction algorithm is also used. The structure and fluid solutions are determined separately, and each solver treats the interaction effects as external forces. This procedure allows the use of existing software and takes advantage of developments that have been made in the structural and fluid fields, independently. To that end, the improved-serial-staggered algorithm originally proposed by Farhat and Lesoinne[31] is applied. Furthermore, a modified multiple moving-frames theory is combined with the nonlinear finite element corotational theory to compute the nonlinear structural response in a flowfield. The Euler equations solved with respect to multiple moving frames of reference are applied to a rigid NACA0012 airfoil with a prescribed pitch motion only and also with coupled pitch and plunge degrees of freedom. To illustrate the application of the proposed algorithm, the two-degrees-of-freedom airfoil with chordwise flexibility is also presented. The proposed algorithm has advantages as it does not require fluid grid regeneration or deformation.

To finalize, nonlinear implicit dynamic algorithms are often instable. To overcome this, the two-dimensional implicit corotational energy-conserving (ICEC) formulation proposed by Crisfield has been adopted.[32,33]

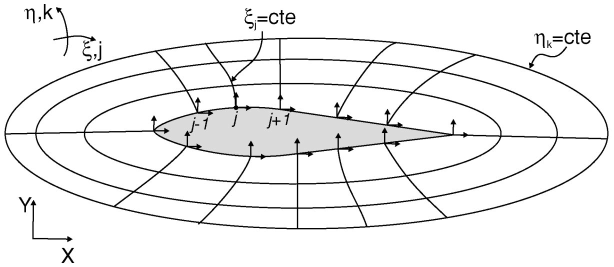

Fig. 1 Multiple frames of reference representation.

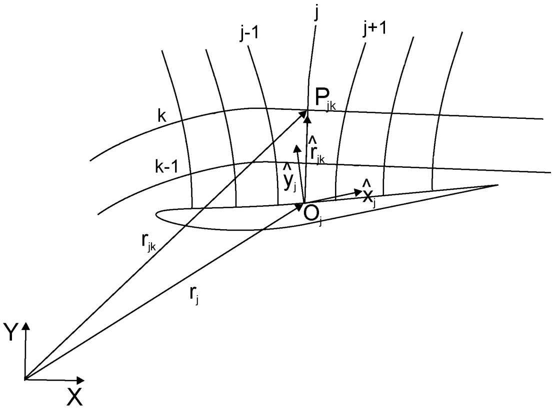

Fig. 2 Fluid particle position vector representation.

II. Fluid Flow Modeling Using Multiple Moving Reference Frames

The basic idea, as first developed by Farhat and Lin[28] and Lin,[20] is to define multiple moving frames of reference, each attached to a structural grid node as presented in Fig. 1.

Each moving frames $(\hat{x}_j, \hat{y}_j)$ is characterized by its origin position vector $\boldsymbol{r}_j$ (see Fig. 2), its orientation, translational velocity $\boldsymbol{V}_j$ and acceleration $\boldsymbol{a}_j$ vectors, and angular velocity $\boldsymbol{\omega}_j$ and acceleration $\dot{\boldsymbol{\omega}}_j$ pseudovectors. As illustrated in Fig. 2, the fluid particle P_{jk} absolute position vector $\boldsymbol{r}_{jk}$ is

$$\boldsymbol{r}_{jk} = \boldsymbol{r}_j + \hat{\boldsymbol{r}}_{jk} \tag{1}$$

where $\boldsymbol{r}_j$ is the respective moving frame origin position and $\hat{\boldsymbol{r}}_{jk}$ the fluid particle position relative to the moving frame j. Differentiating Eq. (1) with respect to time, the P_{jk} absolute velocity $\boldsymbol{V}_{jk}$ is determined and related with the velocity vector $\hat{\boldsymbol{V}}_{jk}$ measured in the moving frame j. Taking into account that the moving frame of reference vectors are time dependent,[34] one obtains

$$\boldsymbol{V}_{jk} = \hat{\boldsymbol{V}}_{jk} + \boldsymbol{V}_j + \boldsymbol{\omega}_j \times \hat{\boldsymbol{r}}_{jk} \tag{2}$$

The last two terms of Eq. (2) represent the effect of the frame motion (translational and rotational), and it will be named as transformation velocity:

$$\boldsymbol{V}_{t,jk} = \boldsymbol{V}_j + \boldsymbol{\omega}_j \times \hat{\boldsymbol{r}}_{jk} \tag{3}$$

The similar relation to Eq. (2) regarding accelerations is

$$\boldsymbol{a}_{jk} = \hat{\boldsymbol{a}}_{jk} + \boldsymbol{a}_j + 2\boldsymbol{\omega}_j \times \hat{\boldsymbol{V}}_{jk} + \dot{\boldsymbol{\omega}}_j \times \hat{\boldsymbol{r}}_{jk} + \boldsymbol{\omega}_j \times (\boldsymbol{\omega}_j \times \hat{\boldsymbol{r}}_{jk}) \tag{4}$$

where a similar transformation acceleration is identified as

$$\boldsymbol{a}_{t,jk} = \boldsymbol{a}_j + 2\boldsymbol{\omega}_j \times \hat{\boldsymbol{V}}_{jk} + \dot{\boldsymbol{\omega}}_j \times \hat{\boldsymbol{r}}_{jk} + \boldsymbol{\omega}_j \times (\boldsymbol{\omega}_j \times \hat{\boldsymbol{r}}_{jk}) \tag{5}$$

From this point further, the subscript jk will be omitted for the sake of simplicity.

A. Euler Equations with Respect to Multiple Moving Frames of Reference

The fluid flow is solved using the two-dimensional partial differential Euler equations in the strong conservation form. Note that the multiple moving-frames theory can also be extended to the Navier–Stokes equations.

The two-dimensional Euler equations relative to multiple moving frames of reference in general curvilinear coordinates[29] are

$$\partial_t \hat{\boldsymbol{Q}} + \partial_\xi \hat{\boldsymbol{E}} + \partial_\eta \hat{\boldsymbol{F}} = \hat{\boldsymbol{S}} \tag{6}$$

where

$$\hat{\boldsymbol{Q}} = J^{-1}\begin{bmatrix} \rho \\ \rho\hat{u} \\ \rho\hat{v} \\ \hat{e} \end{bmatrix}, \qquad \hat{\boldsymbol{E}} = J^{-1}\begin{bmatrix} \rho\hat{U} \\ \rho\hat{u}\hat{U} + \xi_{\hat{x}}p \\ \rho\hat{v}\hat{U} + \xi_{\hat{y}}p \\ \hat{U}(\hat{e}+p) \end{bmatrix}$$

$$\hat{\boldsymbol{F}} = J^{-1}\begin{bmatrix} \rho\hat{V} \\ \rho\hat{u}\hat{V} + \eta_{\hat{x}}p \\ \rho\hat{v}\hat{V} + \eta_{\hat{y}}p \\ \hat{V}(\hat{e}+p) \end{bmatrix}, \qquad \hat{\boldsymbol{S}} = J^{-1}\begin{bmatrix} S_1 \\ S_2 \\ S_3 \\ S_4 \end{bmatrix} \tag{7}$$

Here, ρ is the fluid flow density, $\hat{e}$ the total fluid flow energy relative to the corresponding moving frame of reference, and p the fluid flow pressure

$$p = (\gamma - 1)\left[\hat{e} - \tfrac{1}{2}\rho(\hat{u}^2 + \hat{v}^2) + \tfrac{1}{2}\rho \boldsymbol{V}_t^2\right] \tag{8}$$

J^{-1} the metric Jacobian, and $\xi_{\hat{x}}$, $\xi_{\hat{y}}$, $\eta_{\hat{x}}$, and $\eta_{\hat{y}}$ are the transformation metrics. The contravariant velocities

$$\hat{U} = \xi_{\hat{x}}\hat{u} + \xi_{\hat{y}}\hat{v}, \qquad \hat{V} = \eta_{\hat{x}}\hat{u} + \eta_{\hat{y}}\hat{v} \tag{9}$$

The major difference between the standard Euler equations and the ones derived with respect to multiple frames is the right-hand-side vector $\hat{\boldsymbol{S}}$:

$$S_1 = -\rho\nabla\cdot\boldsymbol{V}_t$$

$$S_2 = -\rho a_{t_x} - \rho\hat{u}\nabla\cdot\boldsymbol{V}_t$$

$$S_3 = -\rho a_{t_y} - \rho\hat{v}\nabla\cdot\boldsymbol{V}_t$$

$$\begin{aligned} S_4 = {}& -\rho[\hat{\boldsymbol{V}}\cdot\boldsymbol{a}_j + (\boldsymbol{\omega}_j \times \hat{\boldsymbol{r}})\cdot\boldsymbol{a}_j + \hat{\boldsymbol{V}}_j\cdot(\boldsymbol{a}_t - \boldsymbol{\omega}_j \times \hat{\boldsymbol{V}}) \\ & + \hat{\boldsymbol{V}}\cdot(\dot{\boldsymbol{\omega}}_j \times \hat{\boldsymbol{r}}) + (\boldsymbol{\omega}_j \times \hat{\boldsymbol{r}})\cdot(\dot{\boldsymbol{\omega}}_j \times \hat{\boldsymbol{r}})] - (\hat{e}+p)\nabla\cdot\boldsymbol{V}_t \end{aligned} \tag{10}$$

B. Numerical Algorithms

A software code to solve the two-dimensional Euler equations with moving frames of reference was developed based on the ARC2D research code.[35,36] The ARC2D was developed based on two-dimensional second-order central finite differences, time-implicit (first- or second-order accurate) algorithm with approximated factorization and implicit operator diagonalization. Second-fourth-order artificial dissipation terms were added.[37]

Considering $\Delta\hat{\boldsymbol{Q}}^n = \hat{\boldsymbol{Q}}^{n+1} - \hat{\boldsymbol{Q}}^n$ and applying a time differencing scheme[38,39] to Eq. (6) rearranged as $\partial_t\hat{\boldsymbol{Q}} = -\partial_\xi\hat{\boldsymbol{E}} - \partial_\eta\hat{\boldsymbol{F}} + \hat{\boldsymbol{S}}$, one has

$$\begin{aligned} \Delta\hat{\boldsymbol{Q}}^n = {}& \frac{\theta\Delta t}{1+\varphi}\left(-\hat{\boldsymbol{E}}_\xi^{n+1} - \hat{\boldsymbol{F}}_\eta^{n+1} + \hat{\boldsymbol{S}}^{n+1}\right) \\ & - \frac{(\theta-1)\Delta t}{1+\varphi}\left(-\hat{\boldsymbol{E}}_\xi^{n} - \hat{\boldsymbol{F}}_\eta^{n} + \hat{\boldsymbol{S}}^{n}\right) \\ & + \frac{\varphi}{1+\varphi}\Delta\hat{\boldsymbol{Q}}^{n-1} + \mathcal{O}\left[\left(\theta - \frac{1}{2} - \varphi\right)\Delta t^2 + \Delta t^3\right] \end{aligned} \tag{11}$$

where θ and φ values are the implicit scheme constants (the three-point implicit scheme is obtained with $\theta = 1$ and $\varphi = 0.5$) and n and $n+1$ represent successive time instants. The terms $\hat{\boldsymbol{S}}^{n+1}$, $\hat{\boldsymbol{E}}^{n+1}$, and $\hat{\boldsymbol{F}}^{n+1}$ are linearized in time as

$$\hat{\boldsymbol{E}}^{n+1} = \hat{\boldsymbol{E}}^{n} + \hat{A}^{n}\Delta\hat{\boldsymbol{Q}}^{n} + \mathcal{O}(\Delta t^2)$$

$$\hat{\boldsymbol{F}}^{n+1} = \hat{\boldsymbol{F}}^{n} + \hat{\boldsymbol{B}}^{n}\Delta\hat{\boldsymbol{Q}}^{n} + \mathcal{O}(\Delta t^2)$$

$$\hat{\boldsymbol{S}}^{n+1} = \hat{\boldsymbol{S}}^{n} + \hat{\boldsymbol{D}}^{n}\Delta\hat{\boldsymbol{Q}}^{n} + \mathcal{O}(\Delta t^2) \tag{12}$$

where $\hat{\boldsymbol{A}} = \partial\hat{\boldsymbol{E}}/\partial\hat{\boldsymbol{Q}}$, $\hat{\boldsymbol{B}} = \partial\hat{\boldsymbol{F}}/\partial\hat{\boldsymbol{Q}}$, and $\hat{\boldsymbol{D}} = \partial\hat{\boldsymbol{S}}/\partial\hat{\boldsymbol{Q}}$ are the flux Jacobians and are explicitly determined by Lin.[29]

Combining Eqs. (11) and (12), one has

$$\left[\boldsymbol{I} + \frac{\theta\Delta t}{1+\varphi}\left(\partial_\xi\hat{\boldsymbol{A}}^n + \partial_\eta\hat{\boldsymbol{B}}^n - \hat{\boldsymbol{D}}^n\right)\right]\Delta\hat{\boldsymbol{Q}}^n$$

$$= \frac{\Delta t}{1+\varphi}\left(-\partial_\xi\hat{\boldsymbol{E}}^n - \partial_\eta\hat{\boldsymbol{F}}^n + \hat{\boldsymbol{S}}^n\right) + \frac{\varphi}{1+\varphi}\Delta\hat{\boldsymbol{Q}}^{n-1} \tag{13}$$

where $\boldsymbol{I}$ is the identity matrix.

Equation (13) is approximated with central differences. One solution to reduce the computational time to solve the problem with a fixed frame[40] is to use an approximate factorization. In the present paper, a similar method is proposed to approximate the left-hand side of Eq. (13) as

$$\text{LHS} = \left(\boldsymbol{I} + \frac{\theta\Delta t}{1+\varphi}\delta_\xi\hat{\boldsymbol{A}}^n\right)\left(\boldsymbol{I} + \frac{\theta\Delta t}{1+\varphi}\delta_\eta\hat{\boldsymbol{B}}^n\right)$$

$$\times\left(\boldsymbol{I} - \frac{\theta\Delta t}{1+\varphi}\hat{\boldsymbol{D}}^n\right)\Delta\hat{\boldsymbol{Q}}^n - \left(\frac{\theta\Delta t}{1+\varphi}\right)^3\delta_\xi\hat{\boldsymbol{A}}^n\delta_\eta\hat{\boldsymbol{B}}^n\hat{\boldsymbol{D}}^n\Delta\hat{\boldsymbol{Q}}^n \tag{14}$$

As $\Delta\hat{\boldsymbol{Q}}^n$ is second order in time, the term $[\theta\Delta t/(1+\varphi^3)]$ can be neglected without reducing the time accuracy. To obtain a more efficient algorithm,[36] the diagonalization is carried out into four scalar operators for the terms $\{\boldsymbol{I} + [\theta\Delta t/(1+\varphi)]\delta_\xi\hat{\boldsymbol{A}}^n\}$ and $\{\boldsymbol{I} + [\theta\Delta t/(1+\varphi)]\delta_\eta\hat{\boldsymbol{B}}^n\}$. Defining $\boldsymbol{\Lambda}_\xi$ and $\boldsymbol{\Lambda}_\eta$ as diagonal matrices, which values are $\hat{\boldsymbol{A}}$ and $\hat{\boldsymbol{B}}$ eigenvalues, and $\boldsymbol{T}_\xi$ and $\boldsymbol{T}_\eta$ as matrices, which columns are $\hat{\boldsymbol{A}}$ and $\hat{\boldsymbol{B}}$ eigenvectors respectively,[41] the relations $\boldsymbol{\Lambda}_\xi = \boldsymbol{T}_\xi^{-1}\hat{\boldsymbol{A}}\boldsymbol{T}_\xi$ and $\boldsymbol{\Lambda}_\eta = \boldsymbol{T}_\eta^{-1}\hat{\boldsymbol{B}}\boldsymbol{T}_\eta$ are valid. Thus, defining $h = \theta\Delta t/(1+\varphi)$, Eq. (14) is rewritten as

$$\text{LHS} = \left[\boldsymbol{T}_\xi\boldsymbol{T}_\xi^{-1} + h\delta_\xi\left(\boldsymbol{T}_\xi\boldsymbol{\Lambda}_\xi\boldsymbol{T}_\xi^{-1}\right)\right]\left[\boldsymbol{T}_\eta\boldsymbol{T}_\eta^{-1} + h\delta_\eta\left(\boldsymbol{T}_\eta\boldsymbol{\Lambda}_\eta\boldsymbol{T}_\eta^{-1}\right)\right]$$

$$\times(I - h\hat{\boldsymbol{D}}^n)\Delta\hat{\boldsymbol{Q}}^n \tag{15}$$

Taking $\boldsymbol{T}_\eta$ and $\boldsymbol{T}_\xi$ out of the spatial derivative, one has

$$\text{LHS} = \boldsymbol{T}_\xi(\boldsymbol{I} + h\delta_\xi\boldsymbol{\Lambda}_\xi)\boldsymbol{T}_\xi^{-1}\boldsymbol{T}_\eta(\boldsymbol{I} + h\delta_\eta\boldsymbol{\Lambda}_\eta)\boldsymbol{T}_\eta^{-1}(\boldsymbol{I} - h\hat{\boldsymbol{D}}^n)\Delta\hat{\boldsymbol{Q}}^n \tag{16}$$

With this simplification, the final system is reduced to blocks so that only 4×4 matrix multiplications and scalar tridiagonal inversions are required. Pulliam and Chaussee[36] showed that for the conventional case with a fixed frame the error induced by this diagonalization reduces the time accuracy to at most first order. However, they also showed that the problem is solved more efficiently as just half the numerical operations are required. The terms $\boldsymbol{\Lambda}_\xi$, $\boldsymbol{\Lambda}_\eta$, $\boldsymbol{T}_\xi$, and $\boldsymbol{T}_\eta$ are determined explicitly. The eigenvalues matrices present the same form as the case with a fixed frame:

$$\boldsymbol{\Lambda}_\xi = \begin{bmatrix} \hat{U} & 0 & 0 & 0 \\ 0 & \hat{U} & 0 & 0 \\ 0 & 0 & \hat{U} + a\sqrt{\xi_{\hat{x}}^2 + \xi_{\hat{y}}^2} & 0 \\ 0 & 0 & 0 & \hat{U} - a\sqrt{\xi_{\hat{x}}^2 + \xi_{\hat{y}}^2} \end{bmatrix} \tag{17}$$

$$\boldsymbol{\Lambda}_\eta = \begin{bmatrix} \hat{V} & 0 & 0 & 0 \\ 0 & \hat{V} & 0 & 0 \\ 0 & 0 & \hat{V} + a\sqrt{\eta_{\hat{x}}^2 + \eta_{\hat{y}}^2} & 0 \\ 0 & 0 & 0 & \hat{V} - a\sqrt{\eta_{\hat{x}}^2 + \eta_{\hat{y}}^2} \end{bmatrix} \tag{18}$$

where a is the sound speed that for ideal fluids is defined as $a^2 = \gamma p/\rho$.

Defining κ as ξ or η, the eigenvectors matrix is

$$\boldsymbol{T}_\kappa = \begin{bmatrix} 1 & 0 & \alpha & \alpha \\ \hat{u} & \tilde{\kappa}_{\hat{y}}\rho & \alpha(\hat{u} + \tilde{\kappa}_{\hat{x}}a) & \alpha(\hat{u} - \tilde{\kappa}_{\hat{x}}a) \\ \hat{v} & -\tilde{\kappa}_{\hat{x}}\rho & \alpha(\hat{v} + \tilde{\kappa}_{\hat{y}}a) & \alpha(\hat{v} - \tilde{\kappa}_{\hat{y}}a) \\ \dfrac{\phi - \varphi}{\gamma - 1} & \rho(\tilde{\kappa}_{\hat{y}}\hat{u} - \tilde{\kappa}_{\hat{x}}\hat{v}) & \alpha\left[\dfrac{\phi + a^2 - \psi}{\gamma - 1} + a\tilde{\Theta}\right] & \alpha\left[\dfrac{\phi + a^2 - \psi}{\gamma - 1} - a\tilde{\Theta}\right] \end{bmatrix} \tag{19}$$

The $\boldsymbol{T}_\kappa$ inverse is

$$\boldsymbol{T}_\kappa^{-1} = \begin{bmatrix} 1 - \dfrac{\phi + \psi}{a^2} & \dfrac{(\gamma - 1)\hat{u}}{a^2} & \dfrac{(\gamma - 1)\hat{v}}{a^2} & -\dfrac{(\gamma - 1)}{a^2} \\ -(\tilde{\kappa}_{\hat{y}}\hat{u} - \tilde{\kappa}_{\hat{x}}\hat{v})/\rho & \dfrac{\tilde{\kappa}_{\hat{y}}}{\rho} & \dfrac{-\tilde{\kappa}_{\hat{x}}}{\rho} & 0 \\ \beta(\phi + \psi - a\tilde{\Theta}) & \beta[\tilde{\kappa}_{\hat{x}}a - (\gamma - 1)\hat{u}] & \beta[\tilde{\kappa}_{\hat{y}}a - (\gamma - 1)\hat{v}] & \beta(\gamma - 1) \\ \beta(\phi + \psi + a\tilde{\Theta}) & -\beta[\tilde{\kappa}_{\hat{x}}a + (\gamma - 1)\hat{u}] & -\beta[\tilde{\kappa}_{\hat{y}}a + (\gamma - 1)\hat{v}] & \beta(\gamma - 1) \end{bmatrix} \tag{20}$$

where $\Theta = \kappa_{\hat{x}}\hat{u} + \kappa_{\hat{y}}\hat{v}$, $\phi = \frac{1}{2}(\gamma - 1)(\hat{u}^2 + \hat{v}^2)$, $\psi = \frac{1}{2}(\gamma - 1)(\boldsymbol{V}_t^2)$, $\alpha = \rho/\sqrt{2}a$, $\beta = \rho/\sqrt{2}\rho a$, $\tilde{\Theta} = \tilde{\kappa}_{\hat{x}}\hat{u} + \tilde{\kappa}_{\hat{y}}\hat{v}$, $\tilde{\kappa}_{\hat{x}} = \kappa_{\hat{x}}/\sqrt{(\kappa_{\hat{x}}^2 + \kappa_{\hat{y}}^2)}$, and $\tilde{\kappa}_{\hat{y}} = \kappa_{\hat{y}}/\sqrt{(\kappa_{\hat{x}}^2 + \kappa_{\hat{y}}^2)}$.

For the sake of completeness, the matrix $\hat{\boldsymbol{D}}$ is presented in the appendix.

Inviscid boundary conditions are considered at the body surface. The pressure is obtained from the momentum equation inner product by the airfoil normal. The locally one-dimensional Riemann invariants boundary conditions are used at the freestream boundary.[42] A far-field circulation correction is also used, which allows the making of the far-field boundary condition closer to the airfoil. Far-field distances of the order of five chords are used without losing accuracy.[35,43]

III. Structure Modeling Using the Finite Element Corotational Theory

The application[29] to illustrate the proposed fluid-structure-interaction method is an infinite length wing structure, thus permitting a two-dimensional analysis. The structure considered is a flexible NACA0012 airfoil stiffened with a vertical rigid shear panel at the quarter-chord as illustrated in Fig. 3. The horizontal spring K_s is set to a high value so that there is no movement in the x direction. Two kind of analysis are performed: first, the airfoil is assumed rigid; next, the airfoil is assumed flexible and its surface is discretized using beam finite elements as illustrated in Fig. 3.

A. Rigid Structure

First, the multiple moving-frame theory is applied to a rigid structure with the purpose of validating the code developed and to compare the results with the case of flexible structure.

The structure motion dimensionless equation[29] is

$$\boldsymbol{M}\ddot{\boldsymbol{q}} + \boldsymbol{K}\boldsymbol{q} = \boldsymbol{F} \tag{21}$$

where the degree of freedom vector is $\boldsymbol{q} = [h/2b \quad \alpha]$, b represents the airfoil semichord, h and α the plunging and the pitching motions respectively, and

$$\boldsymbol{M} = \begin{bmatrix} 1 & \dfrac{x_\alpha}{2} \\ \dfrac{x_\alpha}{2} & \dfrac{\gamma_\alpha^2}{4} \end{bmatrix} \qquad \boldsymbol{K} = \begin{bmatrix} \dfrac{4\omega_h^2 M_\infty^2}{U^{*2}\omega_\alpha^2} & 0 \\ 0 & \dfrac{\gamma_\alpha^2 M_\infty^2}{U^{*2}} \end{bmatrix}$$

$$\boldsymbol{F} = \begin{bmatrix} \dfrac{-2M_\infty^2 C_l}{\pi\mu} \\ \dfrac{2M_\infty^2 C_m}{\pi\mu} \end{bmatrix} \tag{22}$$

Here, U_∞ is the freestream speed, M_∞ is the freestream Mach number, $U^* = U_\infty/b\omega_\alpha$, x_α is the distance in semichord measured from the elastic axis to the center of mass, $\mu = m/\pi\rho b^2$ is the airfoil air mass ratio, m is the airfoil mass, ω_h and ω_α are the plunging and pitching motions uncoupled natural frequencies determined as $\omega_h^2 = K_h/m$, and $\omega_\alpha^2 = K_\alpha/I_\alpha$, $\gamma_\alpha^2 = I_\alpha/(mb^2)$, and I_α is the airfoil polar moment of inertia about the elastic axis. C_l stands for the lift coefficient and C_m for the moment coefficient around the elastic axis. The minus sign on C_l results from the plunge degree of freedom being defined positive downwards. The rotation degree of freedom α is positive clockwise. The time is dimensionless as $t^* = ta_\infty/2b$, where a_∞ is the freestream sound speed. This system is solved using the trapezoidal rule.

B. Flexible Structure

Here, the structure is assumed flexible, and linear and nonlinear simulations are performed. Neglecting the geometric nonlinear effects, the airfoil is discretized using the two-node Hermitian finite element beam with six degrees of freedom

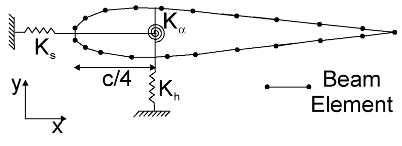

Fig. 3 Wing-like structure.

$$\boldsymbol{p} = \{u_1, v_1, \theta_1, u_2, v_2, \theta_2\} \tag{23}$$

where the subscripts 1 and 2 refer to the beam first and second node respectively, u and v are the translational degrees of freedom in the X and Y directions respectively, and θ is the cross-section rotation. The following dimensionless dynamic equation is solved:

$$\boldsymbol{M}\ddot{\boldsymbol{p}} + \left[M_\infty^2 \big/ (U_\infty/2b)^2\right]\boldsymbol{K}_T\boldsymbol{p} = \left(4b^2\big/a_\infty^2\right)(\boldsymbol{F}_a - \boldsymbol{F}_k) = \boldsymbol{f}_e \tag{24}$$

where $\boldsymbol{M}$ is the finite element lumped mass matrix, $\boldsymbol{K}$ the finite element stiffness matrix, $\boldsymbol{F}_a$ the aerodynamic force vector, $\boldsymbol{F}_k$ the force vector due to the springs reactions, and $\boldsymbol{f}_e$ the total external force. Equation (24) is solved in a stepwise form by determining the solution at each time step based on the solution determined at the previous time step.

The corotational theory is used based on the same beam element to solve for structural geometric nonlinearities. As it was pointed before, in the finite element corotational theory, the current element results from a rigid-body motion of the initial element, resulting in the corotated element, plus an elastic deformation of the corotated element as illustrated in Fig. 4. The initial and current element configurations have lengths of l_0 and l_c, respectively. Each element has a local coordinate system $(\boldsymbol{e}, \boldsymbol{b})$ attached to one of its nodes, and this system continuously rotates with the element. The small elastic deformation is defined relative to this local system, and consequently the linear formulation is valid in it. This formulation is based on Ref. 32.

The tangent stiffness matrix $\boldsymbol{K}$ relates $\delta\boldsymbol{f}_i$ and $\delta\boldsymbol{p}$ as

$$\delta\boldsymbol{f}_i = \boldsymbol{K}_T\delta\boldsymbol{p} \tag{25}$$

where $\boldsymbol{f}_i$ is the element internal force. The displacement vector $\boldsymbol{p}$ in global coordinates represents the total nodal displacement of each finite element, which takes the initial element configuration to the current configuration. The vector $\boldsymbol{p}_L$, relative to the local coordinate system associated with the respective element, represents the nodal elastic deformation undergone by each corotated finite element to obtain the current element configuration. The subscript L is used to identify a variable as local, and no subscript means that the variable is global. The nodal elastic deformation vector relative to the local coordinate system is

$$\boldsymbol{p}_L = \{0, 0, \theta_{L1}, u_L, 0, \theta_{L2}\} \tag{26}$$

where

$$\theta_{L1} = \theta_1 - \alpha, \qquad \theta_{L2} = \theta_2 - \alpha \tag{27}$$

$$u_L = l_c - l_0 = \left[(\boldsymbol{X}_{21} + \boldsymbol{d}_{21})^T(\boldsymbol{X}_{21} + \boldsymbol{d}_{21})\right]^{\frac{1}{2}} - \left[\boldsymbol{X}_{21}^T\boldsymbol{X}_{21}\right]^{\frac{1}{2}} \tag{28}$$

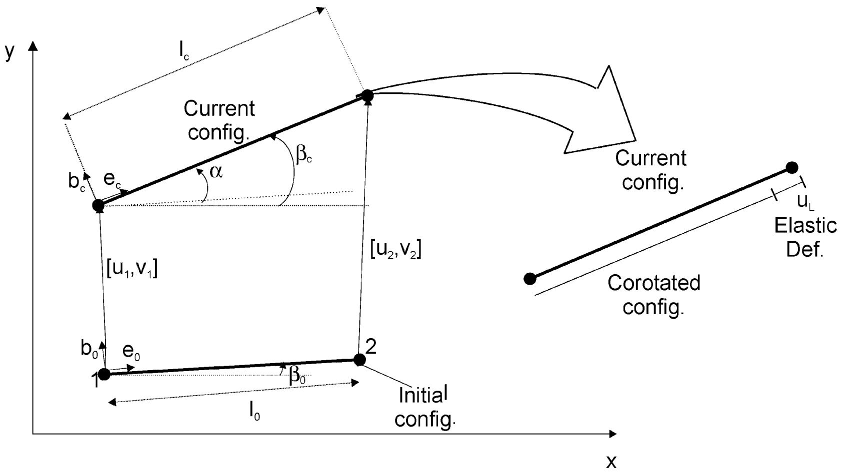

Fig. 4 Initial, corotated, and current configuration representation for a beam element.

Here the subscript 12 applied to a variable refers to the difference between that variable on node 2 and node 1. Therefore, $\boldsymbol{X}_1$ and $\boldsymbol{X}_2$ are the initial element nodal coordinates, $\boldsymbol{X}_{21} = \boldsymbol{X}_2 - \boldsymbol{X}_1$, $\boldsymbol{d} = [u, v]$, $\boldsymbol{d}_{21} = \boldsymbol{d}_2 - \boldsymbol{d}_1$, and α is the element rigid-body rotation obtained from

$$\sin(\alpha) = \frac{\boldsymbol{X}_{21} \times (\boldsymbol{X}_{21} + \boldsymbol{d}_{21})}{l_c l_0} \tag{29}$$

One of the most important steps in the corotational formulation is determining the relation between small changes (virtual) of $\boldsymbol{p}_L$ and small changes of $\boldsymbol{p}$. This relation is generically represented by a transformation matrix $\boldsymbol{T}$ as

$$\delta \boldsymbol{p}_L = \boldsymbol{T} \delta \boldsymbol{p} \tag{30}$$

The element nodal vector of the internal forces in the local system $\boldsymbol{f}_{\mathrm{iL}}$ and the element nodal vector of the internal forces in the global system $\boldsymbol{f}_i$ are related as

$$\boldsymbol{f}_{\mathrm{iL}} = \boldsymbol{T} \boldsymbol{f}_i \tag{31}$$

The vector $\delta \boldsymbol{f}_i$ should be determined to find $\boldsymbol{K}_T$ from Eq. (25). Considering Eq. (31),

$$\delta \boldsymbol{f}_i = \boldsymbol{T}^T \delta \boldsymbol{f}_{\mathrm{iL}} + \delta \boldsymbol{T}^T \boldsymbol{f}_{\mathrm{iL}} \tag{32}$$

The vector $\delta \boldsymbol{f}_{\mathrm{iL}}$ is determined by applying the basic definition of the corotational theory, which states that in the local coordinate system $\delta \boldsymbol{p}_L$ is small, and therefore the elastic deformation $\delta \boldsymbol{p}_L$ can be modeled with a linear finite element. Writing Eq. (25) at the local level

$$\delta \boldsymbol{f}_{\mathrm{iL}} = \boldsymbol{K}_l \delta \boldsymbol{p}_L \tag{33}$$

where $\boldsymbol{K}_l$ is the element linear stiffness matrix. Considering Eqs. (30) and (33), Eq. (32) becomes

$$\begin{aligned} \delta \boldsymbol{f}_i &= \boldsymbol{T}^T \boldsymbol{K}_l \delta \boldsymbol{p}_L + \delta \boldsymbol{T}^T \boldsymbol{f}_{\mathrm{iL}} \\ &= \boldsymbol{T}^T \boldsymbol{K}_l \boldsymbol{T} \delta \boldsymbol{p} + \delta \boldsymbol{T}^T \boldsymbol{f}_{\mathrm{iL}} \end{aligned} \tag{34}$$

The nonlinear tangent stiffness matrix $\boldsymbol{K}_T$ is determined comparing Eqs. (25) and (34). Therefore

$$\boldsymbol{K}_T = \boldsymbol{T}^T \boldsymbol{K}_l \boldsymbol{T} + \boldsymbol{K}_{t\sigma} \tag{35}$$

where $\boldsymbol{K}_{t\sigma}$ verifies the relation

$$\boldsymbol{K}_{t\sigma} \delta \boldsymbol{p} = \delta \boldsymbol{T}^T \boldsymbol{f}_{\mathrm{iL}} \tag{36}$$

The (6×6) transformation matrix $\boldsymbol{T}$ is determined from Eq. (30) from geometric considerations[33]:

$$\delta u_L = \boldsymbol{e}_c^T \delta \boldsymbol{d}_{21} = \boldsymbol{e}_c^T \delta \boldsymbol{d}_2 - \boldsymbol{e}_c^T \delta \boldsymbol{d}_1 \tag{37}$$

$$\delta \theta_{L1} = \delta \theta_1 - \delta \alpha, \qquad \delta \theta_{L2} = \delta \theta_2 - \delta \alpha \tag{38}$$

with

$$\delta \alpha = \left(\boldsymbol{b}_c^T / l_c \right) \delta \boldsymbol{d}_{21} = \left(\boldsymbol{b}_c^T / l_c \right) \delta \boldsymbol{d}_2 - \left(\boldsymbol{b}_c^T / l_c \right) \delta \boldsymbol{d}_1 \tag{39}$$

From Eqs. (30), (37), (38), and (39) it is possible to determine the transformation matrix

$$\boldsymbol{T} = \begin{bmatrix} \multicolumn{4}{c}{0^T} \\ \multicolumn{4}{c}{0^T} \\ \boldsymbol{b}_c^T / l_c & 1 & -\boldsymbol{b}_c^T / l_c & 0 \\ -\boldsymbol{e}_c^T & 0 & \boldsymbol{e}_c^T & 0 \\ \multicolumn{4}{c}{0^T} \\ \boldsymbol{b}_c^T / l_c & 0 & -\boldsymbol{b}_c^T / l_c & 1 \end{bmatrix} \tag{40}$$

where 0^T is a 1×6 zero vector and

$$\boldsymbol{e}_c^T = [\cos(\beta_c), \sin(\beta_c)], \qquad \boldsymbol{b}_c^T = [-\sin(\beta_c), \cos(\beta_c)] \tag{41}$$

β_c is the current configuration angle as illustrated in Fig. 4. The matrix $\delta \boldsymbol{T}$ is

$$\delta \boldsymbol{T} = \begin{bmatrix} \multicolumn{4}{c}{0^T} \\ \multicolumn{4}{c}{0^T} \\ \delta\left(\boldsymbol{b}_c^T / l_c \right) & 0 & -\delta\left(\boldsymbol{b}_c^T / l_c \right) & 0 \\ -\delta \boldsymbol{e}_c^T & 0 & \delta \boldsymbol{e}_c^T & 0 \\ \multicolumn{4}{c}{0^T} \\ \delta\left(\boldsymbol{b}_c^T / l_c \right) & 0 & -\delta\left(\boldsymbol{b}_c^T / l_c \right) & 0 \end{bmatrix} \tag{42}$$

where from Eqs. (41) and (39), and $\delta \beta = \delta \alpha$:

$$\begin{gathered} \delta \boldsymbol{e}_c = \boldsymbol{b}_c \delta \alpha = \left(\boldsymbol{b}_c \boldsymbol{b}_c^T / l_c \right) \delta \boldsymbol{d}_{21} \\ \delta \boldsymbol{b}_c = -\boldsymbol{e}_c \delta \alpha = -\left(\boldsymbol{e}_c \boldsymbol{b}_c^T / l_c \right) \delta \boldsymbol{d}_{21}, \qquad \delta l_c = \boldsymbol{e}_c^T \delta \boldsymbol{d}_{21} \\ \delta(\boldsymbol{b}_c / l_c) = (1/l_c) \delta \boldsymbol{b}_c + \boldsymbol{b}_c \delta(1/l_c) = -\left(\boldsymbol{e}_c \boldsymbol{b}_c^T / l_c^2 + \boldsymbol{b}_c \boldsymbol{e}_c^T / l_c^2 \right) \delta \boldsymbol{d}_{21} \end{gathered} \tag{43}$$

The nonlinear tangential stiffness matrix $\boldsymbol{K}_T$ is determined from Eq. (35). $\boldsymbol{K}_{t\sigma}$ final expression is obtained from Eq. (36), which requires the evaluation of the local internal forces $\boldsymbol{f}_{\mathrm{iL}} = [N, M_1, M_2]$:

$$N = \frac{EA}{l_0} u_L, \qquad \begin{bmatrix} M_1 \\ M_2 \end{bmatrix} = \frac{2EI}{l_0} \begin{bmatrix} 2 & 1 \\ 1 & 2 \end{bmatrix} \begin{bmatrix} \theta_{L1} \\ \theta_{L2} \end{bmatrix} \tag{44}$$

where A is the element cross-sectional area, E the Young's modulus, and I the element moment of inertia.

Combining Eqs. (42–44), and considering Eq. (36), matrix $\boldsymbol{K}_{t\sigma}$ is

$$\boldsymbol{K}_{t\sigma} = \begin{bmatrix} \boldsymbol{K} & -\boldsymbol{K} \\ -\boldsymbol{K} & \boldsymbol{K} \end{bmatrix} \tag{45}$$

where $\boldsymbol{K}$ is the 3×3 matrix:

$$\boldsymbol{K} = \begin{bmatrix} (N/l_c) \boldsymbol{b}_c \boldsymbol{b}_c^T + \left[(M1 + M2) / l_c^2 \right] \left(\boldsymbol{e}_c \boldsymbol{b}_c^T + \boldsymbol{b}_c \boldsymbol{e}_c^T \right) & 0 \\ 0^T & 0 \end{bmatrix} \tag{46}$$

Two algorithms are applied to determine the structure deformation in time. First, the nonlinear version of the trapezoidal rule is adopted. This is a very popular procedure, and, though it is unconditionally stable for linear problems, the same is not true for nonlinear problems. Often for nonlinear systems the trapezoidal rule requires very small time steps to obtain satisfactory solutions, and there is the possibility that the solution can "lock" or "blow up." A very careful solution analysis is required because sometimes the algorithm converges to a solution that is not correct.[44] The solution proposed by Crisfield is an energy-conserving algorithm based on the midpoint rule.[44] This algorithm also uses the information obtained at the midstep $t + \Delta t/2$. Although it might appear more complex and requires larger data storage, the stability and accuracy obtained overcome these inconveniences.

Defining $\boldsymbol{f}_e$ as the external load vector, the total energy change over the time step is

$$\Delta E = \boldsymbol{f}_{\mathrm{it} + \Delta t/2}^T \Delta \boldsymbol{p} + \left[\frac{\dot{\boldsymbol{p}}_{t + \Delta t} - \dot{\boldsymbol{p}}_t}{\Delta t} \right]^T \boldsymbol{M} \Delta \boldsymbol{p} - \boldsymbol{f}_e^T \Delta \boldsymbol{p} \tag{47}$$

This algorithm is stable because it is based on the determination of $\boldsymbol{f}_{\mathrm{it}+\Delta t/2}$. It is not determined from the displacement $\boldsymbol{p}_{t+\Delta t/2}$ but from the $\boldsymbol{f}_{\mathrm{iL},t}$ and $\boldsymbol{f}_{\mathrm{iL},t+\Delta t}$ vectors average.

$$\boldsymbol{f}_{\mathrm{it}+\Delta t/2} = \left\{\left[\boldsymbol{D}\left(\frac{\boldsymbol{T}_t^0 + \boldsymbol{T}_{t+\Delta t}^0}{2}\right)\right]^T + \bar{\boldsymbol{I}}\right\}\left(\frac{\boldsymbol{f}_{\mathrm{iLt}} + \boldsymbol{f}_{\mathrm{iLt}+\Delta t}}{2}\right) \tag{48}$$

Here $\boldsymbol{T}^0$ is the transformation matrix defined in Eq. (40) considering the diagonal unit terms corresponding to the nodal rotation as zero. The $\boldsymbol{D}$ matrix is a correction[32] defined as the diagonal matrix:

$$\mathrm{diag}(\boldsymbol{D}) = \left(0,\, 0,\, \frac{\Delta\alpha}{\sin\Delta\alpha},\, \frac{2}{1+\cos\Delta\alpha},\, 0,\, \frac{\Delta\alpha}{\sin\Delta\alpha}\right) \tag{49}$$

and $\bar{\boldsymbol{I}}$ is a 6×6 matrix, which the only nonzero positions are (3, 3) and (6, 6), which are set to the unity.

The new $\boldsymbol{K}_T$ matrix explicit formula is recalled in the appendix.

IV. Fluid-Structure Interaction

A. Metrics Update

The major advantage of using multiple moving frames is the absence of fluid grid regeneration or deformation. If the structure is considered flexible, only the fluid grid metrics J^{-1}, $\xi_{\hat{x}}$, $\xi_{\hat{y}}$, $\eta_{\hat{x}}$, and $\eta_{\hat{y}}$ need to be updated. The multiple moving-frames method as originally proposed by Lin[29] is based on the assumption of small structural elastic deformations and that each frame reflects the rigid-body motion of the structure. The structural elastic deformations are transferred to the fluid solver by a fast metrics update method. Considering the two-dimensional case, at each node (j, k) each metric is updated:

$$(\Delta\hat{x})_{j,k} = (r_{j,1}/r_{j,k})(\Delta\hat{x})_{j,1}, \qquad (\Delta\hat{y})_{j,k} = (r_{j,1}/r_{j,k})(\Delta\hat{y})_{j,1} \tag{50}$$

where $[\Delta\hat{x}_{j,1}, \Delta\hat{y}_{j,1}]$ is the deformation of the grid point $(j, 1)$ and $r_{j,k}$ the distance between the grid point (j, k) and the airfoil middle chord. Because nodes $(j, 1)$ lie on the surface, $(\Delta\hat{x}_{j,1}, \Delta\hat{y}_{j,1})$ is determined by the structure solver. Equation (50) is based on the idea that the fluid grid points are less affected by the airfoil deformation as they get farthest away.

B. Integrated Corotational Approach

The multiple moving-frames method as originally proposed by Lin[29] and Farhat and Lin[28] was restricted to small elastic deformations because it was assumed that all moving frames had the same orientation of the airfoil's chord (reflecting the airfoil rigid-body motion), and the elastic deformations of the structure were transferred to the fluid algorithm through the metrics update scheme [Eq. (50)]. To assess the effect of large structural deformations, they modeled the coupling between the multiple moving-frames method and a flexible structure with no rigid-body motion by just updating the fluid grid metrics with the structure deformation and preventing the frames to move. For large deformations the method failed.[28]

Here, this limitation is overcome by associating the finite element corotational method with the multiple moving-frames method. Figure 5 illustrates the interaction between these two algorithms, representing a simplified scheme of the fluid grid nodes and the initial and deformed configurations of the structural finite elements. The fluid grid nodes represented are associated with the thicker finite element. This element has attached a moving frame j, which motion reflects this finite element rigid motion evaluated from the corotational finite element equations. The solution of the Euler equations at these fluid grid nodes is determined relative to the frame j. The finite element corotational theory evaluates the moving-frame orientation as $[\boldsymbol{e}_c, \boldsymbol{b}_c]$ from Eq. (41). The origin position $\boldsymbol{r}_j$ of each frame corresponds to the total displacement of the element node where the frame is attached. The finite element corotational method also evaluates the moving frame translational velocity $\boldsymbol{V}_j$ and acceleration $\boldsymbol{a}_j$ vectors and angular velocity $\boldsymbol{\omega}_j$ and angular acceleration $\dot{\boldsymbol{\omega}}_j$ pseudovectors. The finite element current configuration results from small elastic deformations of the corotated finite element. These small elastic deformations will be applied in the fluid grid metrics update scheme [Eq. (50)]. As this deformation is by definition small, the metrics update scheme does not fail.

This method can be extended to three-dimensional problems. In this case, the angular velocity $\boldsymbol{\omega}_j$ and acceleration $\dot{\boldsymbol{\omega}}_j$ vectors have three components different from zero, and the structure is modeled with corotational plates or shell elements. The integrated corotational approach can also be extended to the Navier–Stokes equations.

V. Nonlinear Structural Results

Two nonlinear dynamic structural problems are solved using the trapezoidal rule and the ICEC algorithm with the purpose of illustrating the benefits of the ICEC method.

A. Problem 1: Oscillating Cantilever Beam

This problem is represented in Fig. 6. The initial conditions are presented in the figure, and the structure is subjected to the force of gravity. The problem is solved using four beam elements and a time step of $\Delta t = 0.001$ s. Figure 7 presents the total energy variation obtained with both methods. Figures 8 and 9 present the deformations

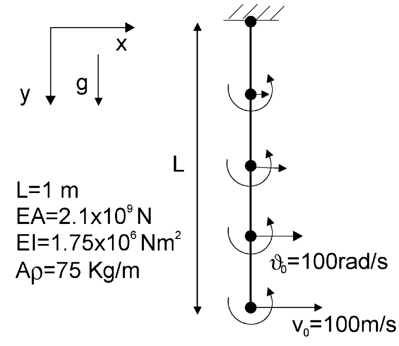

Fig. 6 Problem 1 data.

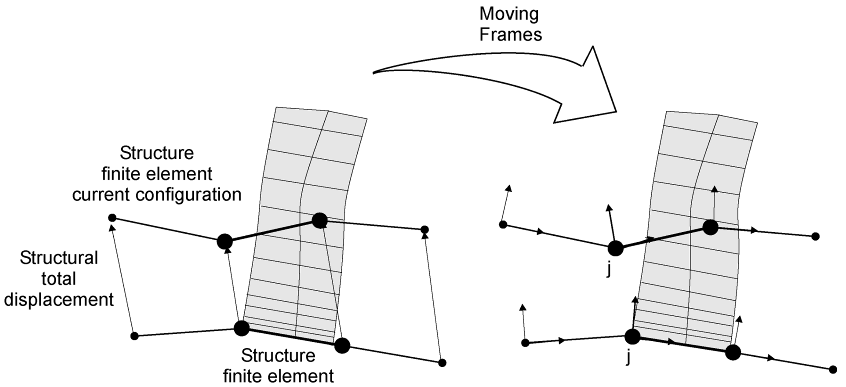

Fig. 5 Corotational approach.

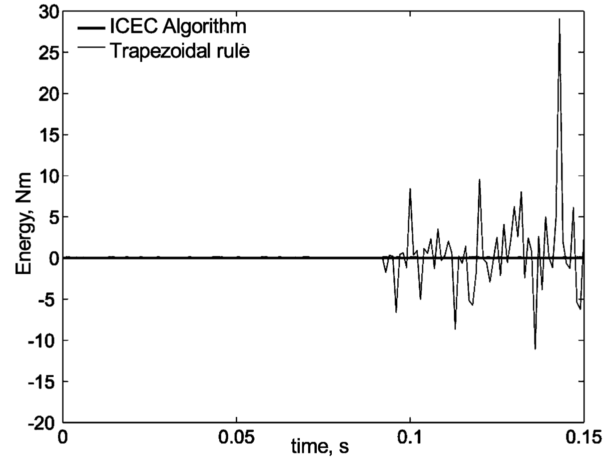

Fig. 7 Problem 1: Total energy change obtained using the nonlinear trapezoidal rule and the ICEC algorithm.

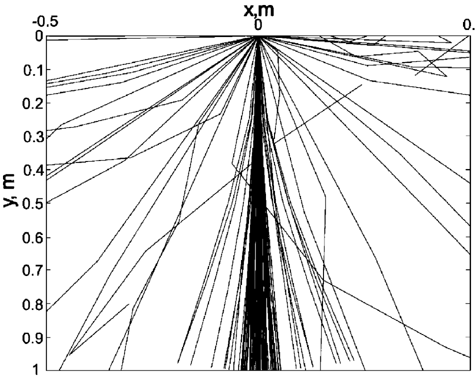

Fig. 8 Problem 1: Dynamic deformation obtained using the nonlinear trapezoidal rule.

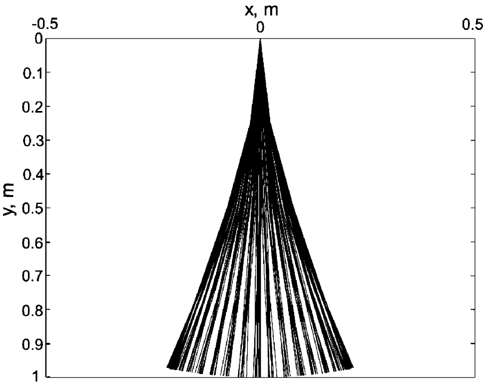

Fig. 9 Problem 1: Dynamic deformation obtained using the ICEC algorithm.

obtained at each time step obtained with the trapezoidal rule and the ICEC algorithm respectively. It can be observed that the trapezoidal rule fails to solve this problem although it converges during the simulation. This failure results from the total energy not being conserved. Using the same data, the ICEC algorithm delivers a stable and accurate solution that agrees with the literature.[32]

B. Problem 2: Free-Free Beam

This problem consists of a free-free four chain system as presented in Fig. 10. Both methods are applied to solve this problem using four beam elements and a time step of $\Delta t = 0.1$ s. Figure 11 presents the total energy variation obtained using the trapezoidal rule. The first configuration presented in Fig. 12 was obtained with the ICEC algorithm, and it agrees with the literature.[32] The chain moves with an anticlockwise rotation and a horizontal movement. The second configuration presented in Fig. 12 was obtained using the trapezoidal rule. This solution matches the configurations obtained with the ICEC algorithm during the first time steps. As observed in Fig. 11, at $t = 4$ s the total energy change increases, and from this instant on the nonlinear trapezoidal rule provides an incorrect solution.

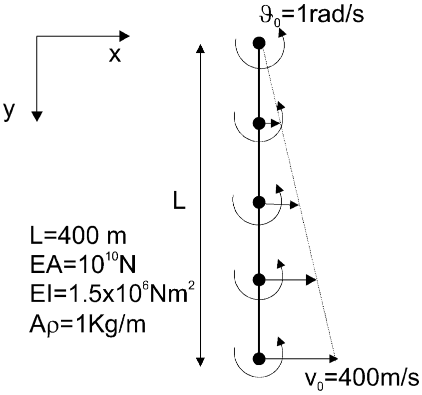

Fig. 10 Problem 2 data.

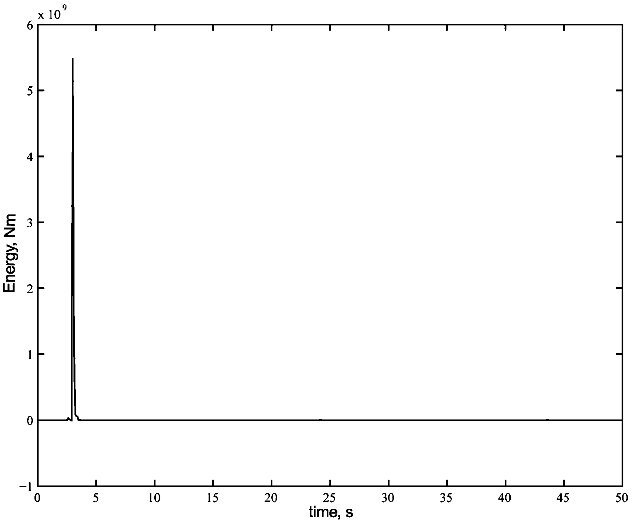

Fig. 11 Problem 2: Total energy change obtained using the trapezoidal rule.

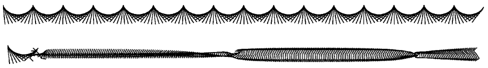

Fig. 12 Problem 2: Chain system configurations obtained using the ICEC and the nonlinear trapezoidal rule.

From these examples, it is recognized that sometimes the nonlinear trapezoidal algorithm converges to a wrong solution. The ICEC algorithm delivers more stable and accurate nonlinear solutions than the nonlinear trapezoidal rule.

VI. Aeroelastic Results with Linear Structures

To validate the multiple moving-frame code developed, some numerical test cases were performed and the results compared with the literature.

A. NACA0012 Airfoil Harmonic Pitching

The NACA0012 airfoil harmonic pitching about the quarter-chord is studied. A grid study was carried out, and it was concluded that a 148×51 O-type grid (see Fig. 13) delivers accurate results. An experimental study of these kind of problems was performed by Landon,[45] and these results are compared with the present numerical procedure results.

A prescribed pitching motion around the airfoil quarter-chord point is applied, and the angle of attack α varies with time according to the relation

$$\alpha(t) = \alpha_m + \alpha_0 \sin(\varpi t) \qquad (51)$$

Table 1 Harmonic NACA0012 airfoil pitch problem data

M_∞	α_m, deg	α_0, deg	k
0.755	0.016	2.51	0.0814
0.6	4.86	2.44	0.081

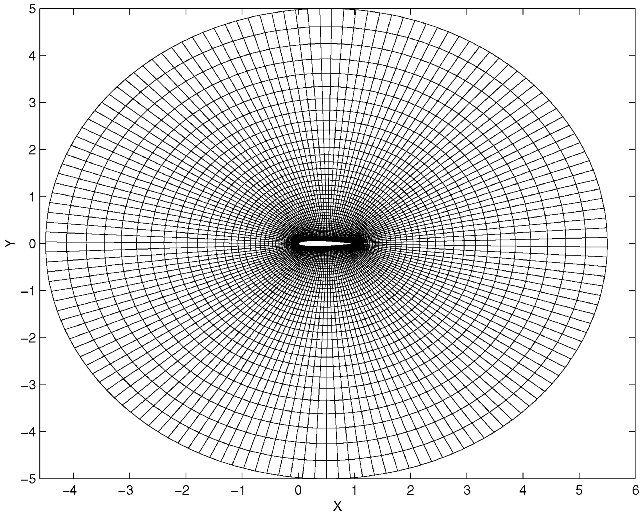

Fig. 13 148 × 51 *O* grid around the NACA0012 airfoil.

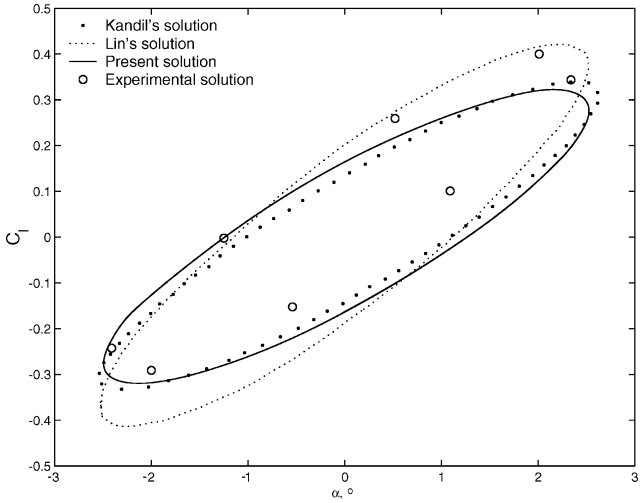

Fig. 14 Lift coefficient vs angle of attack for a harmonic pitch NACA0012 with $M_\infty = 0.755$.

where α_m is the mean angle of attack, α_0 the oscillation amplitude, and defining k as the reduced frequency one has $\varpi = 2M_\infty k$. The initial condition is the steady-state solution at the mean angle α_m. Each reference frame velocity $\boldsymbol{V}_j$ and acceleration $\boldsymbol{a}_j$ vectors are determined based on the airfoil angular velocity $\dot{\alpha}(t)$ and acceleration $\ddot{\alpha}(t)$. Two different cases are solved. Simulation data are presented in Table 1.

Figures 14 and 15 present the lift C_l and moment C_m coefficients variation with the angle of attack α for $M_\infty = 0.755$. The results obtained experimentally[45] are also plotted for comparison purposes, and the inviscid results obtained by Lin[29] using multiple moving frames and Kandil and Chuang[27] using one moving frame located at the quarter-chord are also presented.

The C_l and moment C_m coefficients variations with the angle of attack α for $M_\infty = 0.6$ are presented in Figs. 16 and 17.

It can be inferred that the results obtained are in good agreement with experimental data.[45] Deviations are basically caused by numerical results being based on the inviscid theory, as viscosity and flow separation effects were not considered. The experimental lift and moment coefficients were obtained using integrated pressure data.

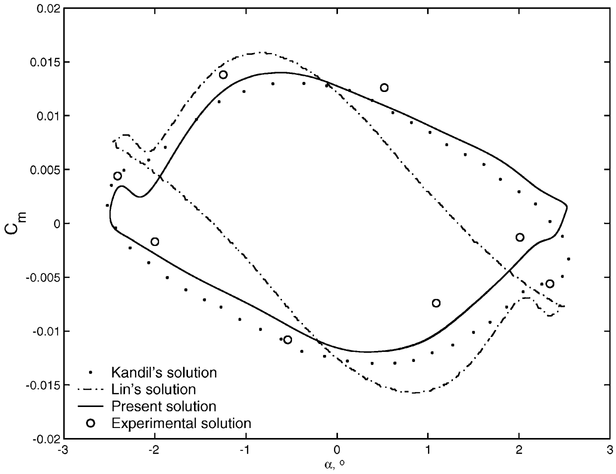

Fig. 15 Moment coefficient vs angle of attack for a harmonic pitch NACA0012 with $M_\infty = 0.755$.

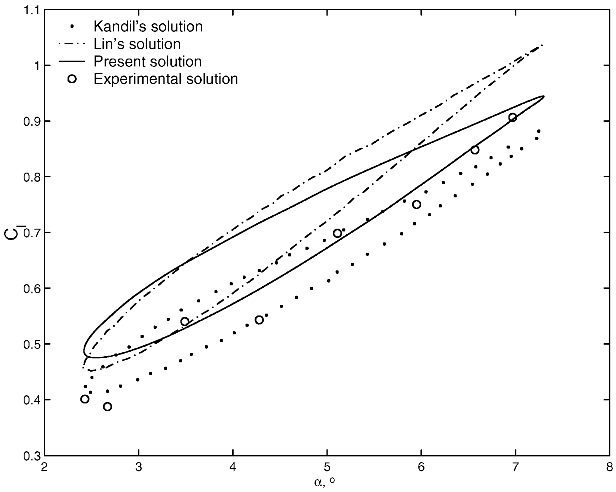

Fig. 16 Lift coefficient vs angle of attack for a harmonic pitch NACA0012 with $M_\infty = 0.6$.

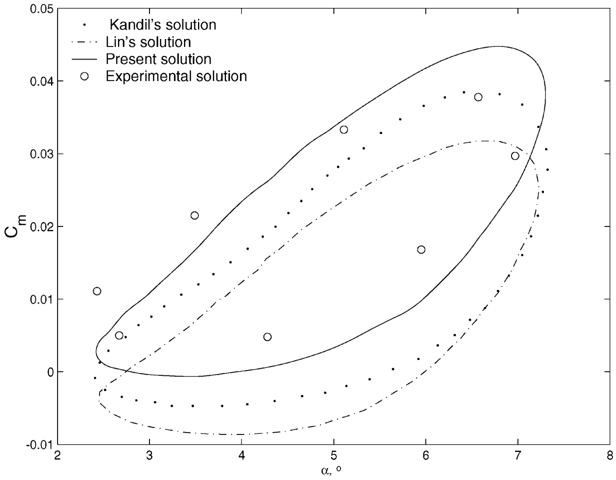

Fig. 17 Moment coefficient vs angle of attack for a harmonic pitch NACA0012 with $M_\infty = 0.6$.

The differences between numerical results are a consequence of differences in the methods to solve the system and implementation, artificial dissipation constants, grid topologies, and time steps. Therefore, the numerical results obtained are consistent with experimental and numerical results presented in the literature. Summarizing, it can be concluded that the multiple moving-frames theory presents good results and the code developed and implemented has been validated for the case with a rigid structure.

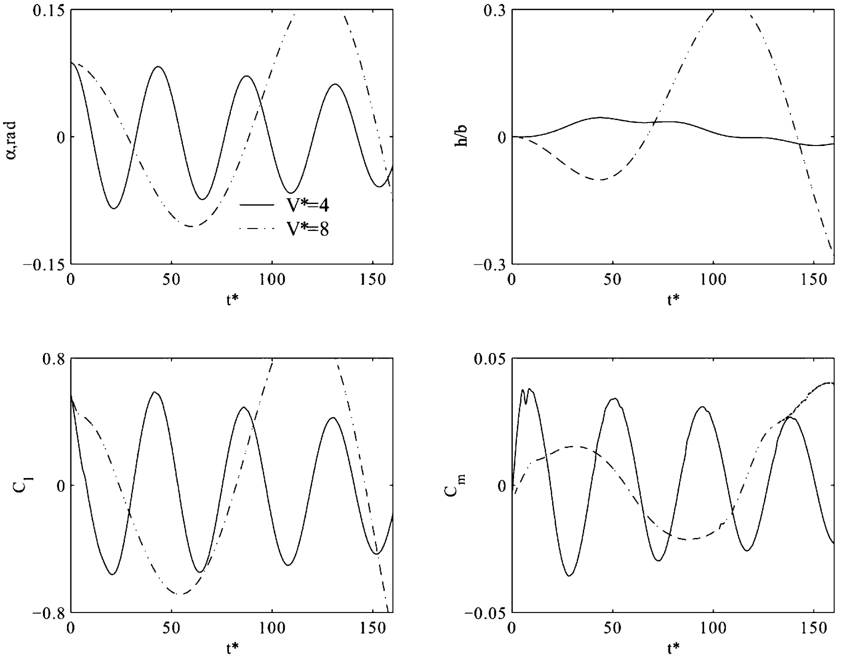

Fig. 18 Pitching α, nondimensional plunge h/b, lift coefficient C_l, and moment coefficient C_m for $U^* = 4$ and 8 and initial angle of attack $\alpha_0 = 5$ deg.

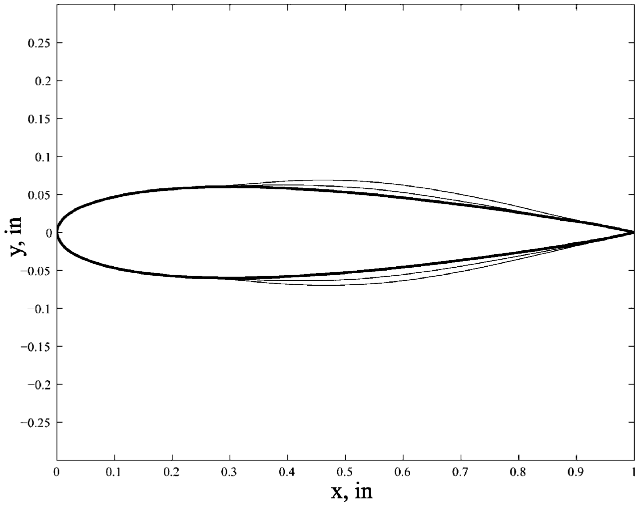

Fig. 19 Airfoil deformation amplified 10 times for $\alpha_0 = 0$ deg and $U_\infty = 7.96$ in./s.

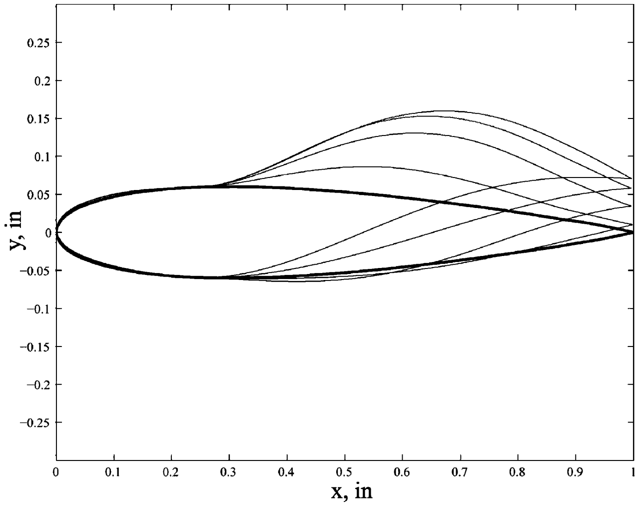

Fig. 20 Airfoil deformation amplified 10 times for $\alpha_0 = 5$ deg and $U_\infty = 7.96$ in./s.

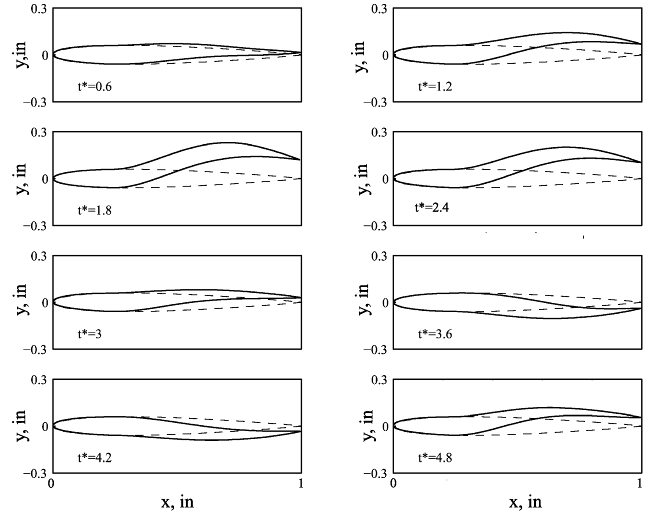

Fig. 21 Airfoil deformation amplified 10 times with $\alpha_0 = 5$ deg and $U_\infty = 7.96$ in./s.

B. NACA0012 Airfoil with Pitch and Plunge Degrees of Freedom

The next test case is a NACA0012 airfoil subjected to a flow with pitch and plunge degrees of freedom. Equation (21) is solved to determine the structure field response. The elastic axis is placed at the quarter-chord, the frequency ratio is $\omega_h/\omega_\alpha = 0.2$, and $\mu = 100$. Results are obtained for dimensionless speeds of $U^* = 4$ and 8 and initial angle of attack $\alpha_0 = 5$ deg. Figure 18 presents the results obtained. Results with $U^* = 4$ are stable, whereas with $U^* = 8$ are unstable. This behavior was also found by Mahajan et al.[46] using the Navier–Stokes equations, the potential theory, and a semi-empirical model. These results demonstrate the coupling between the multiple moving-reference-frame theory and a two-degrees-of-freedom rigid airfoil.

VII. Aeroelastic Results with Nonlinear Structures

The results for an infinite length wing shown in Fig. 3 are presented next. A similar problem was already studied assuming the structure as rigid and flexible/linear by Lin[29] and Farhat and Lin.[28] They considered the airfoil skin total mass was set to unity and the remaining structure properties were assumed constant for all of the beam elements: the airfoil skin thickness was 1% of the chord, and the Young's modulus $E = 10^5$ psi. This Young's modulus is an extreme value that will lead to large structural deformations and to the failure of the original moving-frame method. The airfoil considered is a NACA0012, and it is stiffened at the quarter-chord. The fluid flow Mach number is $M_\infty = 0.8$.

A. Flexible NACA0012 Airfoil Fixed in Space

To illustrate the coupling between the finite element corotational theory and the modified moving-frames method, the springs constants are set to high values to constrain the airfoil rigid-body motion and to allow it just to deform elastically.

Simulations are performed with different initial angles of attack α_0. Initially, the fluid flow steady-state solution is determined considering the initial angle of attack α_0 and after the transient airfoil deformation is obtained. The fluid flow freestream speed is $U_\infty = 7.96$ in./s.

Figure 19 represents some airfoil configurations for the case $\alpha_0 = 0$ deg. For this angle of attack, the upper and the lower airfoil surfaces are under tension, and thus both surfaces distend.

Figure 20 represents the same problem solution but for the case with $\alpha_0 = 5$ deg. For this angle of attack, the upper airfoil surface is under tension, and the lower surface is under compression. As it is expected, the upper surface distends, and the lower surface contracts. Both results qualitatively agree with the physical process involved.

Figure 21 presents the airfoil deformation, amplified 10 times, at different time instants obtained using the nonlinear finite element theory. Using the original multiple moving-frames method,

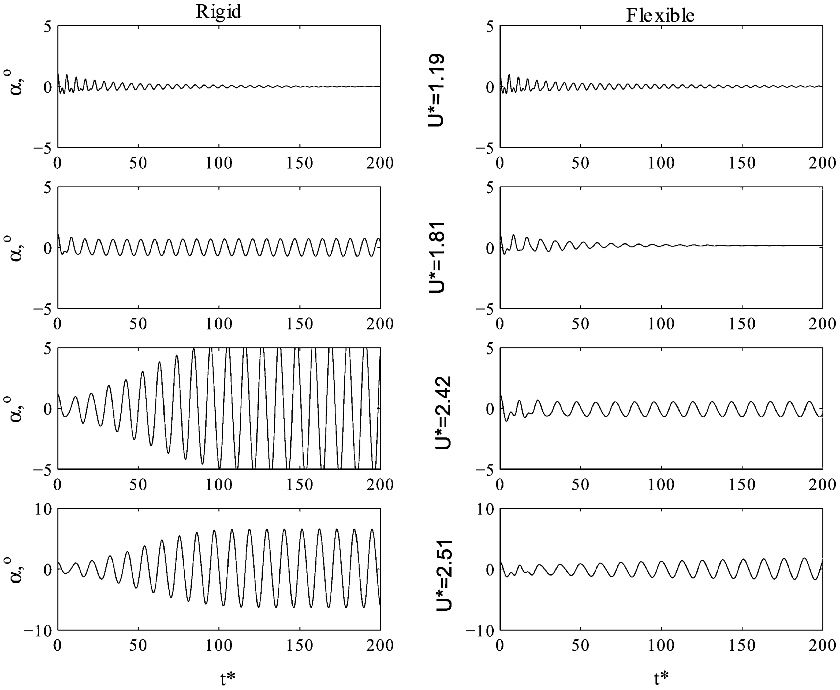

Fig. 22 Aeroelastic results obtained with rigid and nonlinear flexible structure, considering $M_\infty = 0.8$ and $\Delta\alpha = 1.15$ deg.

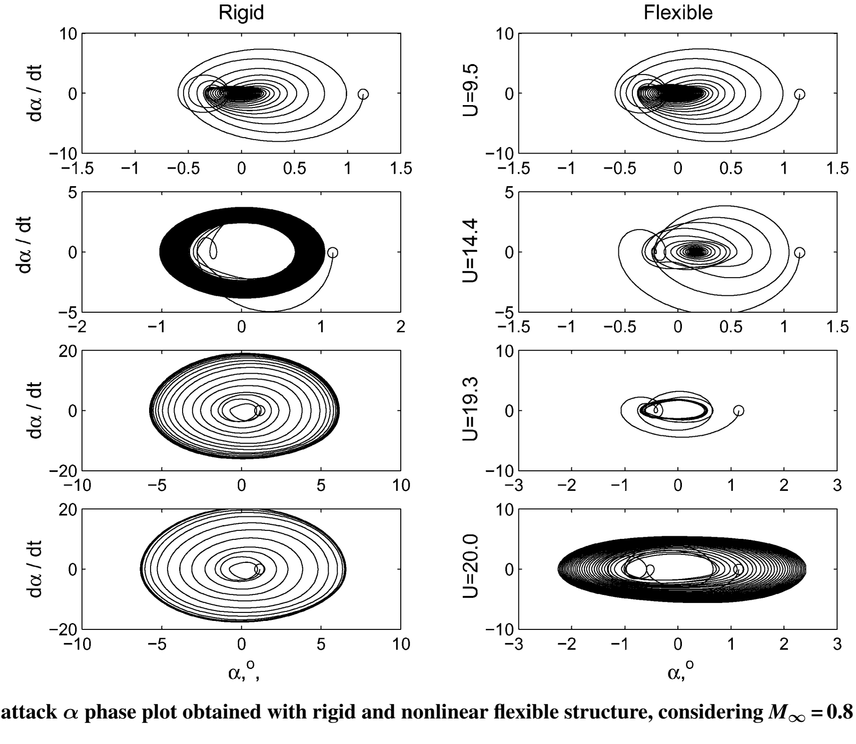

Fig. 23 Angle-of-attack α phase plot obtained with rigid and nonlinear flexible structure, considering $M_\infty = 0.8$ and $\Delta\alpha = 1.15$ deg.

the flow solver failed[28,29] because of large deformations. One concludes that the modified algorithm is able to deal with large elastic deformations.

B. Flexible NACA0012 Airfoil with Pitch and Plunge Degrees of Freedom

The horizontal spring K_s is set to a high value so that there is no movement in the x direction. The remaining springs constants are set as $K_\alpha = 37.167$ and $K_h = 253.3$ (Ref. 28).

It was shown by the authors[47] that it is possible to obtain a solution during a longer simulation range solving the structural problem using the corotational-implicit-energy-conserving algorithm. For the same time step, the structural algorithm fails when it is solved with the trapezoidal rule method, which highlights the importance of the choice of the algorithm to solve the dynamic equations of the structural motion.

An initial $\Delta\alpha = 1.15$ deg pitch-angle perturbation is applied. Figure 22 presents the simulation results for the angle of attack α vs the dimensionless time t^*, for different freestream speeds, considering the structure rigid on the left side, and flexible on the right side. At $U^* = 1.19$ the perturbation is damped. At $U^* = 1.81$ limit-cycle oscillations (LCO) are found for the rigid case. At the same speed, the nonlinear flexible structure solution is still damped. At $U^* = 2.42$, LCO are encountered for the flexible case. At that speed, the rigid case also presents LCO, but its amplitude is larger than in the flexible case. As the freestream speed increases, the LCO amplitude also increases. At $U^* = 2.51$, the flexible results exhibit unstable results, whereas the rigid still exhibits LCO. The LCOs determined using the rigid airfoil have a larger amplitude and are found between the flowfields of $U^* = 1.81$ and 2.51, whereas for the rigid case the LCO are first observed around $U^* = 2.42$. The phase plot of the preceding results is presented in Fig. 23.

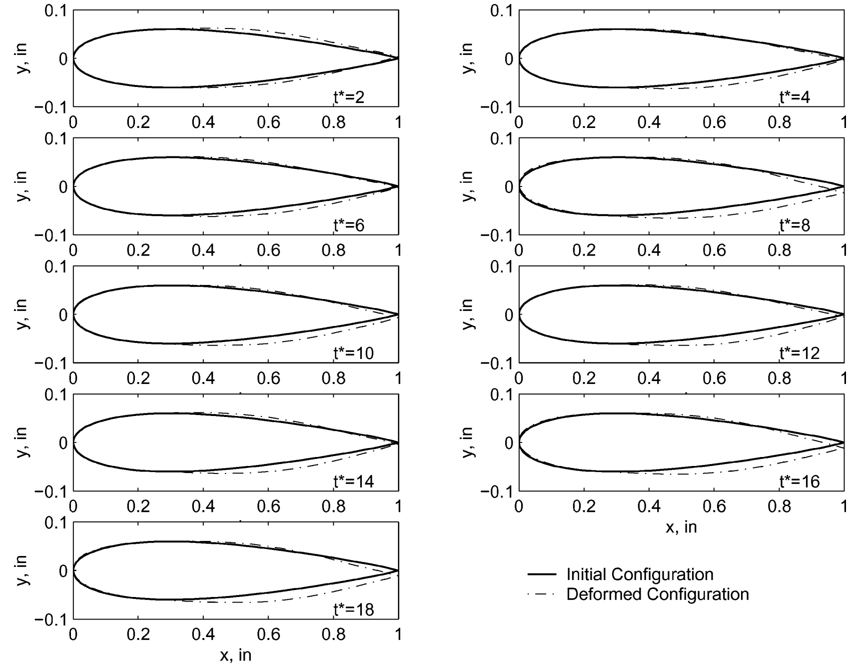

Fig. 24 Airfoil initial and deformed configurations at different time steps for $U^* = 1.81$.

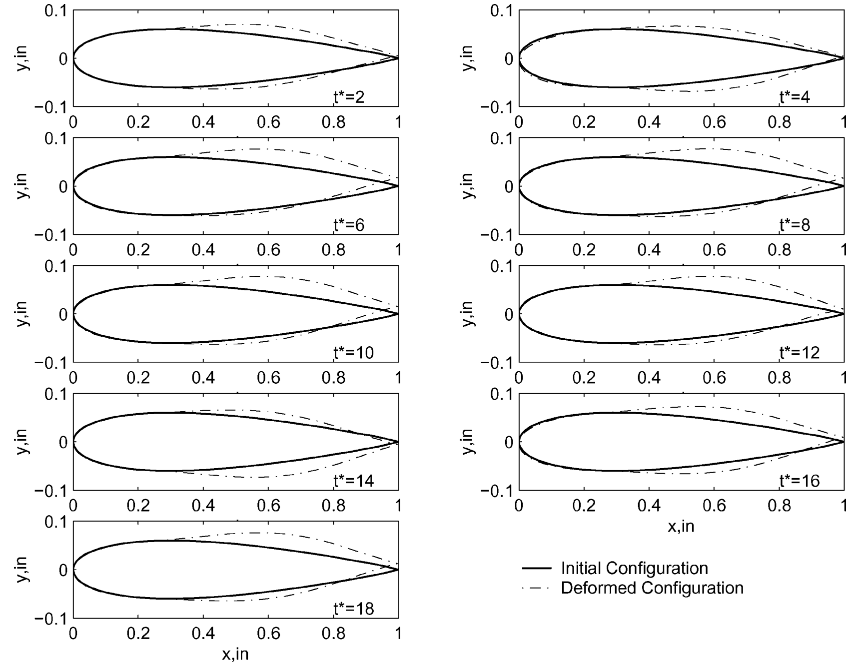

Fig. 25 Airfoil initial and deformed configurations at different time steps for $U^* = 2.42$.

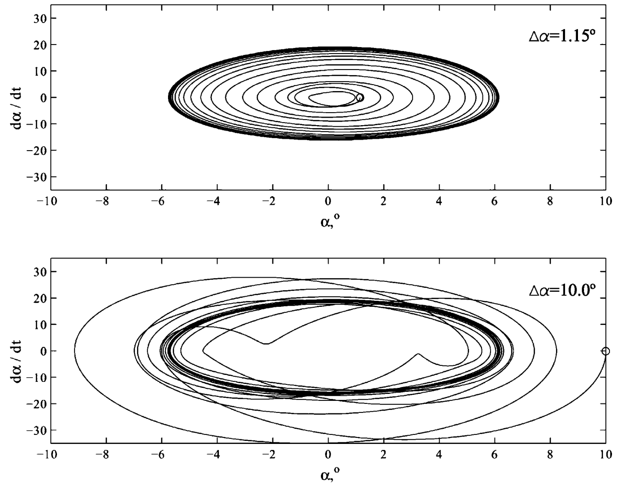

Fig. 26 Angle-of-attack α phase plot obtained with rigid and nonlinear flexible structure, considering $M_\infty = 0.8$, $\Delta\alpha = 1.15$ deg, and $\Delta\alpha = 10.0$ deg.

The importance of modeling nonlinear flexible structures is highlighted in particular for $U^* = 1.81$, where nonlinearities damp the initial perturbation. The initial and deformed airfoil configurations obtained with $U^* = 1.81$ at different time instants are presented in Fig. 24. The airfoil skin deflections for the case with $U^* = 2.42$ are presented in Fig. 25.

A simulation is performed for the case with $U^* = 2.42$ but with an initial perturbation $\Delta\alpha = 10$ deg. These results phase plots are presented in Fig. 26 simultaneously with results for $\Delta\alpha = 1.15$ deg. A stable limit-cycle oscillation is observed as the neighboring trajectories approach the limit cycle.

VIII. Conclusions

This paper presents a formulation of an integrated corotational fluid-structure-interaction framework in the time domain to solve aeroelastic problems with geometrically nonlinear structures in an inviscid flow. The proposed method combines the nonlinear implicit corotational energy-conserving (ICEC) finite element theory to solve the structural field and a method to solve the Euler fluid flow equations using a modified multiple moving-frames method. This method does not require fluid grid regeneration or deformation.

Nonlinear structural dynamic problems were solved, and it was shown that the ICEC method is more stable and accurate than the nonlinear trapezoidal rule. The choice of the algorithm to solve the structural equations is important to numerical stability, which is very important for longer time simulations to verify the long-time response of the structure.

The multiple moving-frame method as originally reported in the literature is restricted to problems with small deformations. The algorithm proposed in this paper overcomes this restriction because the finite element displacement is decomposed into 1) finite element rigid motion, which is transferred to the fluid algorithm through the moving-frame rigid-body motion, and 2) small elastic deformations, which are applied in the metrics update increment. In the original moving-frame method the elastic deformation was applied into the metrics update, and the frames motion reflected the total structure rigid-body motion. The method failed in the presence of large deformations because the update scheme is restricted to small elastic deformations. In the present paper, the frames reflect the finite element rigid motion and not the total structure rigid-body motion. It does not fail for cases with large deformations because the metrics are updated with the elastic deformations determined by the corotational finite element theory, which by definition are small. The present method presents stable solutions for problems where the original method failed. The current formulation of this method is restricted to structured fluid meshes. A straightforward method to associate the fluid grid nodes with a determined moving frame that will allow simulations for complex geometries and unstructured meshes should be developed.

Comparing aeroelastic results between the rigid and the nonlinear flexible structures, it is observed that the chordwise flexibility can play an important role in the system dynamics. For the cases studied, the flexible structure presents limit-cycle oscillations at a higher fluid speed, and its amplitude is smaller compared to the rigid airfoil. The test cases studied agree with the literature.

Appendix: Nonlinear Stiffness Matrix

Matrix D Explicit Form

Assuming that the angular velocity and acceleration vectors just have components in $\hat{z}$ direction and defining the position vector with respect to the moving frame as $\hat{\boldsymbol{r}} = \{\hat{x}, \hat{y}\}$, the $\hat{\boldsymbol{D}}$ Jacobian matrix was determined by Lin[29]:

$$\hat{D}_{12} = \hat{D}_{13} = \hat{D}_{14} = \hat{D}_{24} = \hat{D}_{34} = 0$$

$$\hat{D}_{11} = \hat{D}_{22} = \hat{D}_{33} = -\nabla \cdot \boldsymbol{V}_t, \qquad \hat{D}_{44} = -\gamma \nabla \cdot \boldsymbol{V}_t$$

$$\hat{D}_{21} = -a_{j_x} + \dot{\omega}_j \hat{y} + \omega_j^2 \hat{x}, \qquad \hat{D}_{23} = 2\omega_j$$

$$\hat{D}_{31} = -a_{j_y} - \dot{\omega}_j \hat{x} + \omega_j^2 \hat{y}, \qquad \hat{D}_{32} = -2\omega_j$$

$$\begin{aligned}\hat{D}_{41} = {} & a_{j_x}\omega_j \hat{y} - a_{j_y}\omega_j \hat{x} - v_{j_x} a_{j_x} - v_{j_y} a_{j_y} + v_{j_x}\dot{\omega}_j \hat{y} - v_{j_y}\dot{\omega}_j \hat{x} \\ & + v_{j_x}\omega_j^2 x' + v_{j_y}\omega_j^2 \hat{y} - \omega_j \dot{\omega}_j (\hat{x}^2 + \hat{y}^2) \\ & - \tfrac{1}{2}(\gamma - 1)\big(\hat{u}^2 + \hat{v}^2 + \boldsymbol{V}_t^2\big)\nabla \cdot \boldsymbol{V}_t\end{aligned}$$

$$\hat{D}_{42} = -a_{j_x} - v_{j_y}\omega_j + \dot{\omega}_j \hat{y} + (\gamma - 1)\hat{u}\nabla \cdot \boldsymbol{V}_t$$

$$\hat{D}_{43} = -a_{j_y} + v_{j_x}\omega_j - \dot{\omega}_j \hat{x} + (\gamma - 1)\hat{v}\nabla \cdot \boldsymbol{V}_t \tag{A1}$$

Nonlinear Stiffness Matrix

Next, the total nonlinear stiffness matrix $\boldsymbol{K}_T$ explicit formula,[32] used in the ICEC algorithm, is recalled:

$$\boldsymbol{K}_T = \boldsymbol{K}_1 + \boldsymbol{K}_{T\sigma} \tag{A2}$$

where

$$\boldsymbol{K}_1 = \frac{1}{2}\left\{\left[\boldsymbol{D}\left(\frac{\boldsymbol{T}_t^0 + \boldsymbol{T}_{t+\Delta t}^0}{2}\right)\right]^T + \bar{\boldsymbol{I}}\right\}\boldsymbol{K}_l \boldsymbol{T}_{t+\Delta t} \tag{A3}$$

$$\boldsymbol{K}_{T\sigma} = \begin{bmatrix} A+B+C & -A-B-C \\ -A-B-C & A+B+C \end{bmatrix} \tag{A4}$$

Defining $\Delta\alpha = \alpha_{t+\Delta t} - \alpha_t$, the 3×3 matrices A, B, and C are determined from

$$A = \begin{bmatrix} \dfrac{N_{\text{av}}}{l_{t+\Delta t}(1+\cos\Delta\alpha)}\boldsymbol{f}_{t+\Delta t}\boldsymbol{f}_{t+\Delta t}^T + \dfrac{M_{1\text{av}} + M_{2\text{av}}}{l_{t+\Delta t}^2}\dfrac{\Delta\alpha}{\sin\Delta\alpha}\left(\boldsymbol{e}_{t+\Delta t}\boldsymbol{f}_{t+\Delta t}^T + \boldsymbol{f}_{t+\Delta t}\boldsymbol{e}_{t+\Delta t}^T\right) & 0 \\ 0^T & 0 \end{bmatrix} \tag{A5}$$

$$B = \frac{\sin\Delta\alpha - \Delta\alpha\cos\alpha}{\sin^2\Delta\alpha}\frac{M_{1\text{av}} + M_{2\text{av}}}{2l_{t+\Delta t}}\begin{bmatrix} -\left[\dfrac{\boldsymbol{f}_t}{l_t} + \dfrac{\boldsymbol{f}_{t+\Delta t}}{l_{t+\Delta t}}\right]\boldsymbol{f}_{t+\Delta t}^T & 0 \\ 0^T & 0 \end{bmatrix} \tag{A6}$$

$$C = \frac{\sin\Delta\alpha}{(1+\cos\Delta\alpha)^2}\,\frac{N_{\mathrm{av}}}{l_{t+\Delta t}}\begin{bmatrix}(\boldsymbol{e}_t + \boldsymbol{e}_{t+\Delta t})\boldsymbol{f}^T_{t+\Delta t} & 0\\ 0^T & 0\end{bmatrix} \tag{A7}$$

Acknowledgment

This research was supported by the Fundação para a Ciência e Tecnologia in the framework of the Ph.D. Scholarship SFRH/BD/2786 and the POCTI / EME / 38016 / 2001 project.

References

[1] Dugundji, J., *Computational Nonlinear Mechanics in Aerospace Engineering*, Progress in Astronautics and Aeronautics, Vol. 149, AIAA, Washington, DC, 1992, pp. 531–546.

[2] Dowell, E., Edwards, J., and Strganac, T., "Nonlinear Aeroelasticity," *Journal of Aircraft*, Vol. 40, No. 5, 2003, pp. 857–874.

[3] Virgin, L., and Dowell, E., *Computational Nonlinear Mechanics in Aerospace Engineering*, Progress in Astronautics and Aeronautics, Vol. 149, AIAA, Washington, DC, 1992, pp. 531–546.

[4] Edwards, J., Ashley, H., and Breakwell, J., "Unsteady Aerodynamic Modelling for Arbitrary Motions," *AIAA Journal*, Vol. 17, No. 4, 1979, pp. 365–374.

[5] Livne, E., and Weisshaar, T. A., "Aeroelasticity of Nonconventional Airplane Configurations-Past and Future," *Journal of Aircraft*, Vol. 40, No. 6, 2003, pp. 1047–1065.

[6] Liu, F., Cai, J., Zhu, Y., Wong, A. S. F., and Tsai, H. M., "Calculation of Wing Flutter by Coupled Fluid-Structure Method," *Journal of Aircraft*, Vol. 38, No. 2, 2001, pp. 334–342.

[7] Liu, F., Cai, J., Zhu, Y., Wong, A., and Tsai, H., "Calculation of Wing Flutter by a Coupled CFD-CSD Method," Jan. 2000.

[8] Lee-Raush, E. M., and Batina, J. T., "Wing Flutter Computations Using an Aerodynamic Model Based on the Navier–Stokes Equations," *Journal of Aircraft*, Vol. 33, No. 6, 1996, pp. 1139–1147.

[9] Alonso, J., Martinelli, L., and Jameson, A., "Multigrid Unsteady Navier–Stokes Calculations with Aeroelastic Applications," AIAA Paper 94-0048, 1995.

[10] Alonso, J., and Jameson, A., "Fully-Implicit Time-Marching Aeroelastic Solutions," AIAA Paper 94-0056, 1994.

[11] Zwaan, R., and Prananta, B., "Fluid/Structure Interaction in Numerical Aeroelastic Simulation," *International Journal of Non-Linear Mechanics*, Vol. 37, No. 4, 2002, pp. 987–1002.

[12] Patil, M. J., Hodges, D., and Cesnik, C. E. S., "Nonlinear Aeroelasticity and Flight Dynamics of High-Altitude Long-Endurance Aircraft," *Journal of Aircraft*, Vol. 37, No. 5, 2000, pp. 753–760.

[13] Patil, M., Hodges, D., and Cesnik, C., "Nonlinear Aeroelasticity and Flight Dynamics of High-Altitude Long-Endurance Aircraft," *Journal of Aircraft*, Vol. 38, No. 1, 2001, pp. 88–94.

[14] Garcia, J. A., and Guruswamy, G., "Aeroelastic Analysis of Transonic Wings Using Navier–Stokes Equations and a Nonlinear Beam Finite Element Method," AIAA Paper 99-1215, 1999.

[15] Tang, D., Dowell, E., and Hall, C., "Limit Cycle Oscillation of Cantilevered Wing in Low Subsonic Flow," *AIAA Journal*, Vol. 37, No. 3, 1999, pp. 364–371.

[16] Weiliang, Y., and Dowell, E., "Limit Cycle Oscillation of a Fluttering Cantilever Plate," *AIAA Journal*, Vol. 29, No. 11, 1991, pp. 1929–1936.

[17] Dowell, E., and Tang, D., "Nonlinear Aeroelasticity and Unsteady Aerodynamcis," *AIAA Journal*, Vol. 40, No. 9, 2002, pp. 1697–1707.

[18] Sheta, E., Harrand, V., Thompson, D., and Strganac, T., "Computational and Experimental Investigation of Limit Cycle Oscillations of Nonlinear Aeroelastic Systems," *Journal of Aircraft*, Vol. 39, No. 1, 2002, pp. 133–141.

[19] Piperno, S., "Numerical Methods Used in Aeroelasticity Simulations," CERMICS-INRIA, Tech. Rept. ceramics-92-5, Sophia-Antipolis Cedex, France, Feb. 1992.

[20] Guruswamy, G., "Unsteady Aerodynamic and Aeroelastic Calculations for Wings Using Euler Equations," *AIAA Journal*, Vol. 28, No. 3, March 1990, pp. 461–469.

[21] Kim, D.-H., and Lee, I., "Transonic and Low-Supersonic Aeroelastic Analysis of a Two-Degree-of-Freedom Airfoil with Free-Play Non-Linearity," *Journal of Sound and Vibration*, Vol. 234, No. 5, 2000, pp. 859–888.

[22] Soulaïmani, A., BenElhajAli, A., and Feng, Z., "A Distributed Computing Methodology for Nonlinear Aeroelasticity," AIAA Paper 21-0868, Jan. 2002.

[23] Piperno, S., "Explicit/Implicit Fluid/Structure Staggered Procedures with a Structural Prediction and Fluid Subcycling for 2D Inviscid Aeroelastic Simulations," *International Journal for Numerical Methods in Fluids*, Vol. 25, No. 10, 1997, pp. 1207–1226.

[24] Geuzaine, P., Grandmont, C., and Farhat, C., "Design and Analysis of ALE Schemes with Provable Second-Order Time-Accuracy for Inviscid and Viscous Flow Simulations," *Journal of Computational Physics*, Vol. 191, No. 1, 2003, pp. 206–227.

[25] Farhat, C., Geuzaine, P., and Brown, G., "Application of a Three-Field Nonlinear Fluid-Structure Formulation to the Prediction of the Aeroelastic Parameters on a F-16 Fighter," *Computers and Fluids*, Vol. 32, No. 1, 2003, pp. 3–29.

[26] Kandil, O. A., and Chuang, H. A., "Computation of Steady and Unsteady Vortex-Dominated Flows with Shock Waves," *AIAA Journal*, Vol. 26, No. 5, 1988, pp. 524–531.

[27] Kandil, O. A., and Chuang, H. A., "Unsteady Airfoil Computation Using Implicit Euler Scheme on Body-Fixed Grid," *AIAA Journal*, Vol. 27, No. 8, 1989, pp. 1031–1037.

[28] Farhat, C., and Lin, T. Y., "Transient Aeroelastic Computations Using Multiple Moving Frames of Reference," AIAA Paper 90-3053-CP, 1990.

[29] Lin, T.-Y., "A Multiple Frames of Reference Approach to Aeroelastic Computations: Application to Airfoil Flutter Analysis," Ph.D. Dissertation, Dept. of Aerospace Engineering Sciences, Univ. of Colorado, Boulder, CO, 1990.

[30] Relvas, A., "Computational Fluid-Structure Interaction Modelling of Nonlinear Aeroelastic Structures," Master's Thesis, Dept. of Mechanical Engineering, Univ. of Victoria, Victoria, BC, Canada, Dec. 2002.

[31] Farhart, C., and Lesoinne, M., "Two Efficient Staggered Algorithms for the Serial and Parallel Solution of the Three-Dimensional Nonlinear Transient Aeroelastic Problems," *Computer Methods in Applied Mechanics and Engineering*, Vol. 182, No. 4, 2000, pp. 499–515.

[32] Galvanetto, U., and Crisfield, M., "An Energy-Conserving Co-Rotational Procedure for the Dynamics of Planar Beam Structures," *International Journal for Numerical Methods in Engineering*, Vol. 39, No. 13, 1996, pp. 2265–2282.

[33] Crisfield, M., *Non-Linear Finite Element Analysis of Solids and Structures*, Vol. 1, Wiley, West Sussex, U.K., 1991.

[34] Meriam, J. L., and Kraige, L. J., *Engineering Mechanics, Vol. 2: Dynamics*, 4th ed., Wiley, New York, 1997.

[35] Pulliam, T., "Notes on Solution Methods in Computational Fluid Dynamics," von Karman Inst. for Fluid Mechanics Lecture Series, Rhode-St-Genese, Belgium, Jan. 1986.

[36] Pulliam, T., and Chaussee, D., "A Diagonal Form of an Implicit Approximate-Factorization Algorithm," *Journal of Computational Physics*, Vol. 39, No. 2, 1981, pp. 347–363.

[37] Pulliam, T. H., "Artificial Dissipation Models for the Euler Equations," *AIAA Journal*, Vol. 24, No. 12, 1986, pp. 1931–1940.

[38] Beam, R. M., and Warming, R. F., "An Implicit Factored Scheme for the Compressible Navier–Stokes Equations," *AIAA Journal*, Vol. 16, No. 4, 1978, pp. 393–402.

[39] Beam, R., and Warming, R. F., "An Implicit Finite-Difference Algorithm for Hyperbolic Systems in Conservation Law Form," *Journal of Computational Physics*, Vol. 22, 1976, pp. 87–110.

[40] Beam, R., and Warming, R., "An Implicit Finite-Difference Algorithm for Hyperbolic Systems in Conservative Form," *Journal of Computational Physics*, Vol. 22, No. 1, 1976, pp. 87–110.

[41] Warming, R. F., Beam, R. M., and Hyett, B. L., "Diagonalization and Simultaneous Symmetrization of the Gas-Dynamic Matrices," *Mathematics of Computations*, Vol. 29, No. 132, Oct. 1975, pp. 1037–1045.

[42] Hirsch, C., *Numerical Computation of Internal and External Flows, Vol. II: Computational Methods for Inviscid and Viscous Flows*, Wiley, West Sussex, U.K., 1988.

[43] Thomas, J. L., and Salas, M. D., "Far-Field Boundary Conditions for Transonic Lifting Solutions to the Euler Equations," *AIAA Journal*, Vol. 24, No. 7, 1986, pp. 1074–1080.

[44] Crisfield, M., and Shi, J., "A Co-Rotational Element/Time-Integration Strategy for Non-Linear Dynamics," *International Journal for Numerical Methods in Engineering*, Vol. 37, No. 11, 1994, pp. 1897–1913.

[45] Landon, R., "NACA0012 Oscillatory and Transient Pitching in Compendium of Unsteady Aerodynamic Measurements," AGARD Tech. Rept. R-702, Paris, Aug. 1982.

[46] Mahajan, A., Kaza, K., and Dowell, E., "Semi-Empirical Model for Prediction of Unsteady Forces on an Airfoil with Application to Flutter," *Journal of Fluids and Structures*, Vol. 7, No. 1, Jan. 1993, pp. 87–103.

[47] Relvas, A., and Suleman, A., "Application of Corotational Theory to Nonlinear Aeroelasticity," *Proceedings of the Fourth International Conference on Engineering Computational Technology*, edited by B. Topping and C. M. Soares, Civil-Comp Press, U.K., 2004; also *Computer and Structures* (submitted for publication).